Investigation of the wake characteristics of an underwater vehicle with and without a propeller

Zhideng Zhou, Zhaobin Li, Xiaolei Yang *, Shizhao Wang, Duo Xu

The State Key Laboratory of Nonlinear Mechanics, Institute of Mechanics, Chinese Academy of Sciences, Beijing 100190, China
School of Engineering Sciences, University of Chinese Academy of Sciences, Beijing 100049, China

ARTICLE INFO

ABSTRACT

In this work, we investigate the wake characteristics of an underwater vehicle (i.e., the DARPA Suboff submarine model) using large-eddy simulation with the hull and appendages represented by the curvilinear immersed boundary method, and the propeller parameterized using an actuator disk (AD) model. Two cases with and without the AD propeller are carried out. The results show that the near wake for the case with the AD propeller is featured by an inner velocity-deficit region mainly due to the hull, a jet from the propeller, and an outer velocity-deficit region mainly caused by the fins and the sail. In the far wake, the interaction between the propeller's jet and the sail's wake dominates the upper region. As for the turbulence statistics, the peak magnitudes and positions of the Reynolds stresses and the levels of the power spectral density at certain frequencies are affected by the AD propeller in different ways at different downstream locations.

1. Introduction

Wakes are of interest in numerous practical applications, such as airplanes, cars, ships, and underwater vehicles. The present work is focused on the wake of the Defense Advance Research Projects Agency's (DARPA) Suboff submarine model (Groves et al., 1989), a notional geometry for investigating hydrodynamics of underwater vehicles. The flows around this vehicle surface are featured by flow structures over a variety of scales, ranging from small protrusions on the surface to the scales of the propeller and the hull. The computational demand is high for capturing all the relevant scales, especially when the far wake evolution is of interest. In this work, we employ a sharp interface immersed boundary method with a wall model to simulate the flow over the hull with appendages, and an actuator disk model to model the effect of the propeller as shown in Fig. 1, with a focus on the characteristics in the far wake of the DARPA Suboff model.

In the literature, the flow over the Suboff model or its variants have been carried out in a number of experimental and numerical studies (Huang et al., 1994; Jiménez et al., 2010a; Posa and Balaras, 2016; Liu et al., 2021b). Huang et al. (1994) conducted experiments on the flow over the stern on several Suboff model configurations, both with and without appendages. Their measurements showed that the boundary layer on the stern is strongly affected by the adverse pressure gradient. Jiménez et al. (2010a) conducted experiments on the wake turbulence of an axisymmetric Suboff-like body over a wide range of Reynolds numbers in a wind tunnel, revealing self-similarity

of the mean velocity profiles in both midline plane and planes away from the midline plane. The self-similarity of the second-order statistics (e.g., the Reynolds stresses), on the other hand, was not observed up to 15 diameters downstream from the stern, and the statistics were strongly affected by the necklace vortices trailing from the base of the fins in the near wake. The evolution of the intermediate wake was also compared with those from experiments on the Suboff model with stern fins (Jiménez et al., 2010b), showing that the fins yielded velocity deficits in the outer region of the wake and increasing turbulence intensities behind the fin tips. Overall, these experiments demonstrated the complex dynamics of the near wake, especially for cases of Suboff model with appendages. Furthermore, the unavoidable support for the experimental Suboff model imposes extra influence on the flow statistics, e.g., the asymmetry of the wake, the reduced level of turbulence intensities, and the shear stress, as reported in the literature (Jiménez et al., 2010a,b).

Large-eddy simulation (LES) has been employed in the literature for predicting and understanding the wake characteristics of the Suboff model. Kumar and Mahesh (2018) employed wall-resolved large-eddy simulation (WRLES) to capture the near-wall flow structures and the wake evolution on a bare Suboff model at $Re = 1.1 \times 10^6$ (the Reynolds number based on the free-stream velocity and the length of the body). Consistent with the experimental results (Jiménez et al., 2010a), the self-similarity in the mean streamwise velocity was observed in their
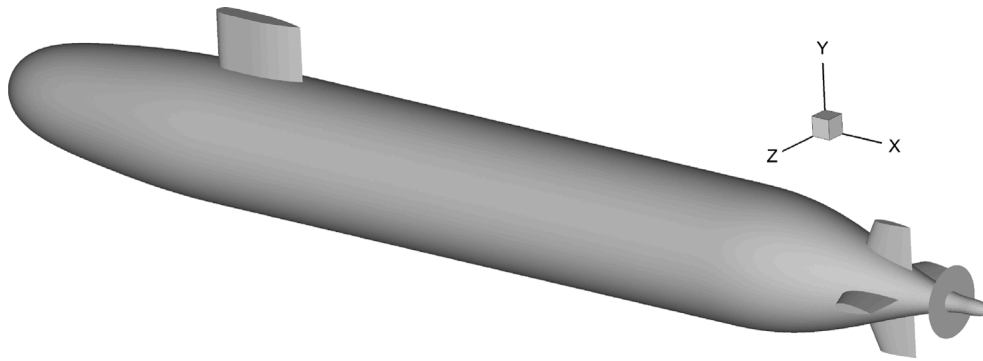

Fig. 1. The geometry of the DARPA Suboff model with appendages and an actuator disk for the propeller.

simulation results. Zhou et al. (2020) performed an LES of the turbulent flow over an axisymmetric body of revolution with the length-to-diameter ratio of 3.17 at $Re = 1.9 \times 10^6$, found that the tail-cone boundary layer behaved more like an axisymmetric wake and the velocity statistics agreed with the experimental data (Hickling et al., 2019). As for the Suboff with appendages, Posa and Balaras (Posa and Balaras, 2016) reported a WRLES at $Re = 1.2 \times 10^6$, found that the shear layer from the trailing edge of the fins significantly affects the wake characteristics and observed a bimodal distribution in the profiles of Reynolds stresses. To reveal the Reynolds number effects on the structure of the boundary layer over the stern and the near wake, Posa and Balaras (2020) carried out LES of the flow around the Suboff model with appendages up to $Re = 1.2 \times 10^7$. They found that the growth of the boundary layer thickness over the stern due to the adverse pressure gradient is almost independent of the Reynolds number. In the near wake, the bimodal distribution of the turbulent stresses is very similar for the two Reynolds numbers considered. However, it is still prohibitively expensive to employ the WRLES for the hydrodynamics at full scale of a practical ship, for which the Reynolds number can be as high as 10^9 (Stern et al., 2013; Liu et al., 2021a), because of the extremely high resolution required to resolve the viscous scale near the wall.

Wall-modeled large-eddy simulation (WMLES), in which the small-scale turbulence near the wall is modeled, provides a computationally affordable way for simulating the flow over the Suboff model at high Reynolds numbers. Alin et al. (2010) reviewed the WMLES, detached eddy simulation (DES), and Reynolds-averaged Navier–Stokes (RANS) for simulating the flow around the Suboff model with and without appendages, and showed that the WMLES gives the best representation of the flow structures and the second-order statistics of velocity. Subsequently, Liefvendahl and Fureby Liefvendahl and Fureby (2017) reviewed the grid resolution requirements for WRLES and WMLES for ship hull hydrodynamics at both model and full-scale. WMLES was also employed for certain parts of the Suboff model (e.g., the flow along the mid-body) in WRLES (Posa and Balaras, 2020; Zhou et al., 2020). WMLES on the flows around a bare hull model was carried out by Shi et al. (2019). A good agreement with experimental results was observed for the pressure and the skin-friction coefficients on the body and the streamwise velocity in the wake.

Another challenge in simulating the far wake of the Suboff model is caused by the propeller. In the literature, the flow through a propeller has been simulated with different fidelities. Balaras et al. (2015) employed 3.3 billion grid nodes in a geometry-resolved WRLES of the INSEAN E1619 propeller under open water condition and captured the dynamics of the tip vortices and their footprint on the statistics of the wake. Kumar and Mahesh (2017) simulated the wake of a five-bladed propeller using WRLES on unstructured grids and analyzed the phase-averaged and azimuthal-averaged flow fields in detail. Posa and Broglia (2022) reported the LES of a system of a marine propeller and a hydrofoil using 4 billion grid nodes, in which a detailed analysis

of the overall wake is presented, especially the turbulent fluctuations. Even for the Suboff model with appendages and a propeller, Posa and Balaras (2018) reported the WRLES results at $Re = 1.2 \times 10^6$ in towed and self-propelled conditions using 2.8 and 3.5 billion nodes, respectively. The comparison showed that the boundary layer over the mid-body is almost unaffected by the propeller, but the bimodal distribution of turbulent stresses in the near wake is replaced by an axial peak, caused by the instability of the hub vortex. Using WMLES with the curvilinear immersed boundary (CURVIB) method, Liao et al. (2020b) simulated the flow around a propeller in crashback mode, in which the propeller rotates in the reverse direction to decelerate an advancing underwater vehicle. They found that the requirements of grid resolution are different for accurately predicting different flow quantities, in which the side-force coefficient and mean velocity are less sensitive than the thrust force coefficient and turbulence kinetic energy (TKE), and are different for different regions, that the near wake region and the region around the blade are more sensitive than the far wake region. To alleviate the grid requirement for geometry-resolved simulations, Liao et al. (2020a) proposed an actuator surface model for LES of propeller wake, which employs a separate RANS simulation to compute the force coefficients on the surface and apply the obtained force to the actuator surface of the propeller.

In this work, we investigate the wake characteristics of the Suboff model with/without a propeller up to six-hull-length downstream using a multi-fidelity method (Zhou et al., 2021), in which the hull with appendages is simulated using the curvilinear immersed boundary method and the propeller is parameterized using an actuator disk model. We first show the global flow statistics of the Suboff model with appendages and then investigate the effect of the propeller on the wake characteristics by examining the time-averaged flow fields.

The rest of the paper is organized as follows. In Section 2, the LES solver, the CURVIB method, and the actuator disk model employed in this work are briefly described. The simulation setup of the cases is shown in Section 3. The obtained results are then presented in Section 4. At last, the conclusions are drawn in Section 5.

2. Methodology

In this section, we describe the employed multi-fidelity method including the CURVIB method for simulating the turbulent flow around the hull with appendages in Section 2.2 and the actuator disk model for modeling the propeller in Section 2.3.

2.1. LES solver

We employ the Virtual Flow Simulator (VFS-Wind) (Yang et al., 2015b,a; Calderer et al., 2015) code for LES of the turbulent flows. The

governing equations are the three-dimensional, unsteady, spatially filtered incompressible Navier–Stokes equations in non-orthogonal, generalized curvilinear coordinates, shown as follows:

$$\frac{1}{J}\frac{\partial U^i}{\partial t} = \frac{\xi_l^i}{J}\left(-\frac{\partial}{\partial \xi^j}(U^j u_l) + \frac{\mu_f}{\rho_f}\frac{\partial}{\partial \xi^j}\left(\frac{g^{jk}}{J}\frac{\partial u_l}{\partial \xi^k}\right)\right.$$
$$\left. -\frac{1}{\rho_f}\frac{\partial}{\partial \xi^j}\left(\frac{\xi_l^j p}{J}\right) - \frac{1}{\rho_f}\frac{\partial \tau_{lj}}{\partial \xi^j} + f_l\right), \tag{1}$$

$$J\frac{\partial U^j}{\partial \xi^j} = 0, \tag{2}$$

where $i, j, l = 1, 2$ and 3 represents the x, y, and z axis respectively. J is the Jacobian determinant of the transformation matrix, x_i and ξ^i represent the Cartesian and curvilinear coordinates, respectively. $\xi_l^i = \partial\xi^i/\partial x_l$ represents the transformation metric of the coordinates. u_i is the ith component of the velocity vector in Cartesian coordinates. $U^i = (\xi_m^i/J)u_m$ is the contravariant volume flux. $g^{jk} = \xi_l^j\xi_l^k$ represents the contravariant metric tensor. ρ_f, μ_f and p are the density, the dynamic viscosity and the pressure, respectively. f_l represents the body force introduced by the actuator disk model and the immersed boundary method. In the momentum equation, τ_{lj} represents the anisotropic part of the subgrid-scale (SGS) stress tensor, which is modeled by the dynamic eddy viscosity model,

$$\tau_{lj} - \frac{1}{3}\tau_{kk}\delta_{lj} = -2\nu_t\overline{S}_{lj}, \tag{3}$$

where $\overline{S}_{lj}$ is the filtered strain-rate tensor and ν_t is the eddy viscosity calculated by

$$\nu_t = C\Delta^2|\overline{S}|, \tag{4}$$

where C is the model coefficient calculated dynamically using the procedure of Germano et al. (1991), $|\overline{S}| = \sqrt{2\overline{S}_{lj}\overline{S}_{lj}}$ and $\Delta = J^{-1/3}$ is the filter size, where J^{-1} is the cell volume.

The governing equations are discretized in space using the second-order central difference scheme and advanced in time using the second-order accurate fractional step method. An algebraic multigrid acceleration along with generalized minimal residual method (GMRES) solver is used to solve the pressure Poisson equation. A matrix-free Newton–Krylov method is used for solving the discretized momentum equation. More details about the flow solver can be found in the literature (Ge and Sotiropoulos, 2007; Kang et al., 2011; Yang et al., 2015b).

2.2. The CURVIB method

The curvilinear immersed boundary method (Gilmanov and Sotiropoulos, 2005; Ge and Sotiropoulos, 2007) is employed to simulate the effect of the hull with appendages on the surrounding flow, in which the governing equations are discretized and solved on non-body-fitted grids. For variants of the CURVIB method developed for different applications, readers can refer to these papers (Borazjani et al., 2008; Khosronejad et al., 2011; Kang et al., 2011; Le and Sotiropoulos, 2013; Gilmanov et al., 2015).

In the CURVIB method, the surface of the solid body is discretized using unstructured triangular meshes superposed on the background grid. The background grid nodes in general do not coincide with the surface meshes, that the boundary conditions cannot be applied directly. According to the location with respect to the position of the body, the background grid nodes are classified into the fluid nodes and the solid nodes. The solid nodes that fall inside the body are blanked out from the simulation. The fluid nodes that are located in the fluid but with at least one neighbor in the solid are further identified as the IB nodes, where the boundary conditions are applied.

For direct numerical simulation and wall-resolved LES, the velocity at the IB nodes can be interpolated from the fluid nodes and the velocity at the boundary in the wall-normal direction. For wall-modeled LES, the

linear interpolation is not suitable. In the present study, the simplified thin boundary layer equation is solved in the wall-normal direction on a one-dimensional grid to compute the wall shear stress, which is written as

$$\frac{\partial}{\partial y}\left[(\nu + \nu_t)\frac{\partial u}{\partial y}\right] = 0, \tag{5}$$

where y is the coordinate in the wall-normal direction, u is the wall-tangential velocity, and ν_t is the turbulent viscosity modeled using the mixing-length model with the van Driest damping function. With the computed wall shear stress, the flux at the control surface next to the IB node is constructed to serve as the boundary conditions for the outer flow simulations (Yang et al., 2010).

2.3. Actuator disk model

The actuator disk model is employed to take into account the effect of propeller on the flow. The force of the propeller $\mathbf{F}_{propeller}$ is determined by the instantaneous hydrodynamic drag $\mathbf{F}_{drag}$ of Suboff and the acceleration, which can be expressed as follows:

$$\mathbf{F}_{propeller} = \mathbf{F}_{drag} + M\frac{d\mathbf{V}}{dt}, \tag{6}$$

where M and $\mathbf{V}$ are the mass and the velocity of the Suboff, respectively. The obtained thrust force is then distributed on a disk with an equivalent radius. In the present work, a relatively simple situation is considered, that (1) the acceleration of the Suboff is zero; (2) the force distribution on the actuator disk is assumed to be uniform; (3) only the hydrodynamic force in the axial direction is considered, i.e., the tangential force exerted by the propeller rotation is neglected. The obtained force on the actuator disk is spread to the surrounding background grid nodes using the smoothed discrete delta function (Yang et al., 2009).

Employing an actuator-disk representation of the propeller was based on the following reasons: (1) Our previous work of a different propeller (Liao et al., 2020a) has shown that the tip vortices are only prevalent in the very near wake, and the rotational motion of the wake become less significant in the far wake at about 11 diameters downstream of the propeller; (2) The information of the propeller for the DARPA suboff is not available, which prohibits the use of advanced models, e.g., the actuator surface model or the geometry-resolved method, in this work.

3. Simulation setup

In this section, the setup for the simulated cases is presented. As seen in Fig. 1, the bare hull of the DARPA Suboff is axis-symmetric and is consists of a streamlined forebody, a parallel middle body, and a stern with contraction in the radial direction. The appendages consist of a sail and four stern fins. The propeller, modeled using the actuator disk, is placed downstream of the fins. The radius ($r = 0.258D$) and the position ($x = 8.225D$) of the actuator disk are set according to Özden et al. (2016), where D denotes the diameter of the middle body.

In order to simulate the far wake in a computationally efficient way, two separate simulations, i.e., a simulation with the Suboff model and a simulation for the far wake, were carried out. In the simulation with the Suboff model, the Reynolds number based on the length of the Suboff $L = 8.6D$ is equal to $Re = U_0 L/\nu = 1.2 \times 10^7$, where U_0 denotes the velocity of incoming flow, ν denotes the kinematic viscosity of the fluid. At the inlet, a uniform inflow superimposed with the velocity fluctuations (the turbulence intensity is approximately 1%), which are generated using a synthetic turbulence approach Mann (1998), is imposed. Free-slip boundary condition is imposed on the computational boundaries in the spanwise and vertical directions. At the outlet, the Neumann boundary condition is employed.

The Suboff model is placed at zero angle of attack and zero yaw angle with respect to the inflow, as shown in Fig. 2. The origin of the coordinate system coincides with the nose of the hull. In this
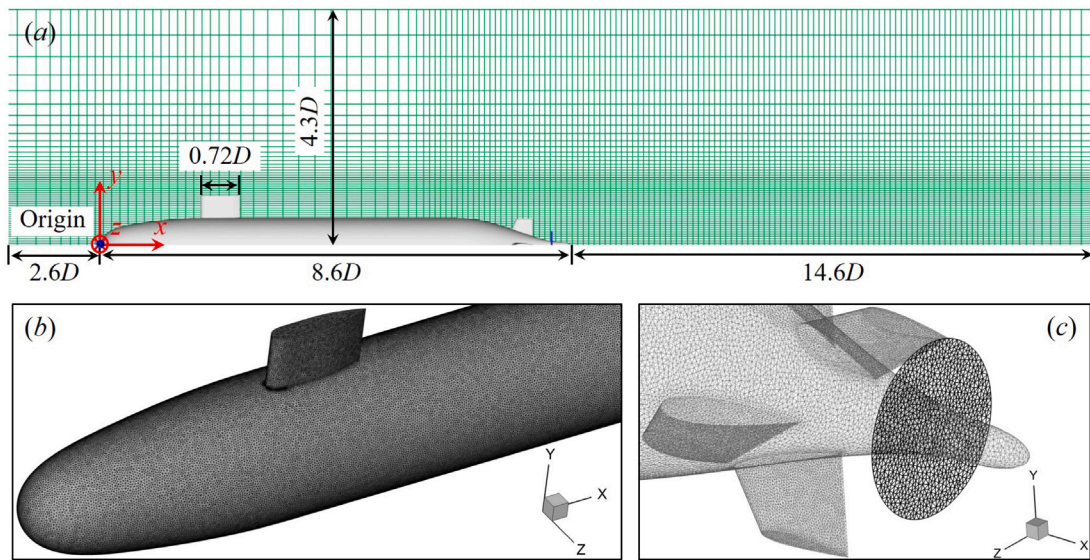
Fig. 2. (a) Computational domain with the xOy plane of the Cartesian background grid (1 in every 5 nodes is shown) and the Suboff model with appendages; (b) the unstructured surface mesh for the Suboff model with sail; (c) the unstructured surface mesh for the actuator disk and fins.

Table 1
Details of the grid spacing (Δh) and number of grid nodes (N) at different locations. For the grid spacing, "u" denotes the uniform grid, "r" and "l" denote the non-uniform grid defined using the tanh function, with the smallest grid cell on the right and left side, respectively.

$x/D \in$	[−2.6, −0.4]	[−0.4, 2.0]	[2.0, 6.0]	[6.0, 16.0]	[16.0, 23.2]
N	35	80	90	500	135
$\Delta h/D$	0.03 (r)	0.03 (u)	0.03 (l)	0.02 (u)	0.02 (l)
			0.02 (r)		
$y/D \in$	[−4.3, −1.2]		[−1.2, 1.2]		[1.2, 4.3]
N	100		300		100
$\Delta h/D$	0.008 (r)		0.008 (u)		0.008 (l)
$z/D \in$	[−4.3, −1.2]		[−1.2, 1.2]		[1.2, 4.3]
N	100		300		100
$\Delta h/D$	0.008 (r)		0.008 (u)		0.008 (l)

coordinate system, the sail approximately occupies the region $[1.82D,$ $2.54D] \times [0.495D, 0.905D] \times [−0.066D, 0.066D]$, in the streamwise ($x$), vertical ($y$) and spanwise ($z$) directions, respectively. The region $[7.49D, 7.89D] \times [0.162D, 0.48D] \times [−0.041D, 0.041D]$ is occupied by the upper stern fin, and the other three stern fins are located at 90, 180 and 270 degrees in the azimuthal directions, respectively. The extent of the computational domain in the streamwise, vertical and spanwise directions is $[−2.6D, 23.2D] \times [−4.3D, 4.3D] \times [−4.3D, 4.3D]$, with grid numbers $841 \times 501 \times 501$. The grid is locally refined near the Suboff model and stretched outwards. Table 1 shows the number of grids and grid spacings in different regions.

For the far wake simulations, the computational domain is extended to approximately $6.0L$ downstream. The inflow is obtained from the flow fields at $x/D = 16.0$ of the simulation with Suboff model. The mesh for the wake simulation is coarser in the crosswise directions as there is no need to resolve the boundary layer around the Suboff model. Table 2 shows the details of the computational domain, the grid spacing, and the number of grids at different locations. The computational cost of the simulations is shown in Appendix A. To test the grid dependence of the simulation results, the WMLES results on the grid (medium) in Table 1 are compared with those from the simulations on a coarse grid and fine grid in Appendix B.

Table 2
Details of the computational domain, grid spacing (Δh) and number of grids (N) at different locations for the continuous wake simulation. The symbol notations are similar to Table 1.

$x/D \in$		[16.0, 60.0]	
N		1100	
Δh		0.04 (u)	
$y/D \in$	[−4.3, −0.6]	[−0.6, 0.6]	[0.6, 4.3]
N	60	60	60
Δh	0.02 (r)	0.02 (u)	0.02 (l)
$z/D \in$	[−4.3, −0.6]	[−0.6, 0.6]	[0.6, 4.3]
N	60	60	60
Δh	0.02 (r)	0.02 (u)	0.02 (l)

4. Results and discussion

4.1. Global flow field

In this section, we compare the flow fields around the Suboff model with/without the propeller. Fig. 3 compares the pressure and friction coefficients obtained from the present WMLES with/without AD propeller. These coefficients are defined as follows:

$$C_p = \frac{P - P_{\text{ref}}}{\frac{1}{2}\rho U_0^2}, \qquad C_f = \frac{\langle \tau_w \rangle}{\frac{1}{2}\rho U_0^2}, \tag{7}$$
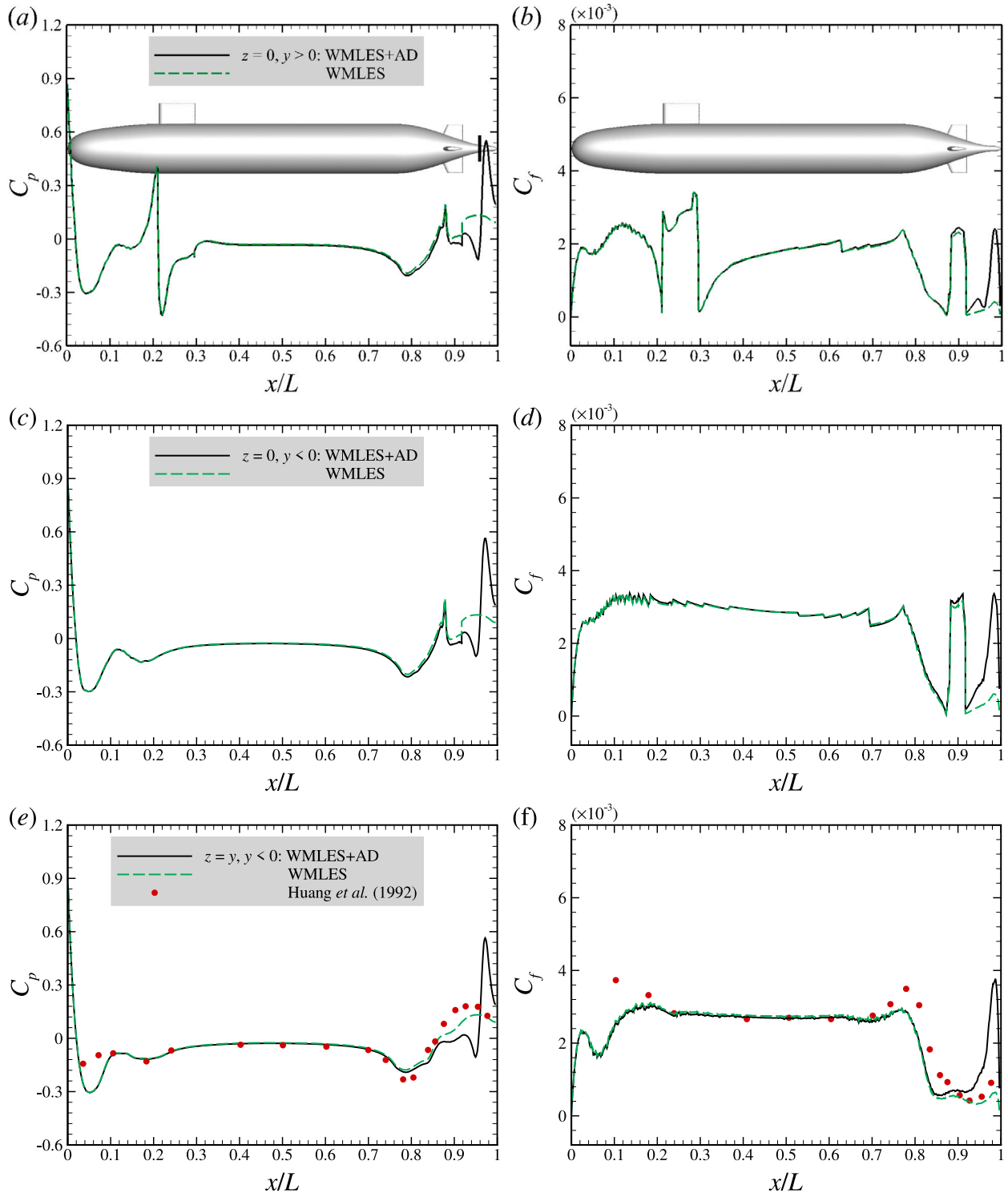
Fig. 3. Comparisons of pressure coefficient C_p and skin-friction coefficient C_f obtained from the present WMLES of the Suboff model with and without AD, and experiment of Huang et al. (1994) at different profiles: (a~b) $z = 0, y > 0$, (c~d) $z = 0, y < 0$ and (e~f) $z = y, y < 0$.

where P is the time-averaged pressure and $P_{ref} = 0$ is the reference pressure in the far field, τ_w denotes the wall shear stress. When post-processing the results to compute C_f, we calculate τ_w using the Werner–Wengle (WW) model (Werner and Wengle, 1993), which provides an explicit way for computing τ_w and is similar to the wall model employed in WMLES.

In Figs. 3(a)–(f), both the C_p and C_f exhibit good consistency between the cases with and without the AD propeller at most parts of the hull surface, indicating that the disk has a minor influence on the

upstream flow surrounding the hull. The major differences are located near the disk ($x/L \approx 0.956$), with an increased C_p and C_f in the region behind the disk caused by the pressure jump and velocity acceleration due to the AD propeller. In front of the disk, the C_p is decreased, while the C_f is slightly increased.

When comparing the present simulation with the experimental results, the C_p computed from the case without the AD propeller, in general, agrees with that in the literature (Huang et al., 1994), as shown in Fig. 3(e). The only difference is observed at the fore part
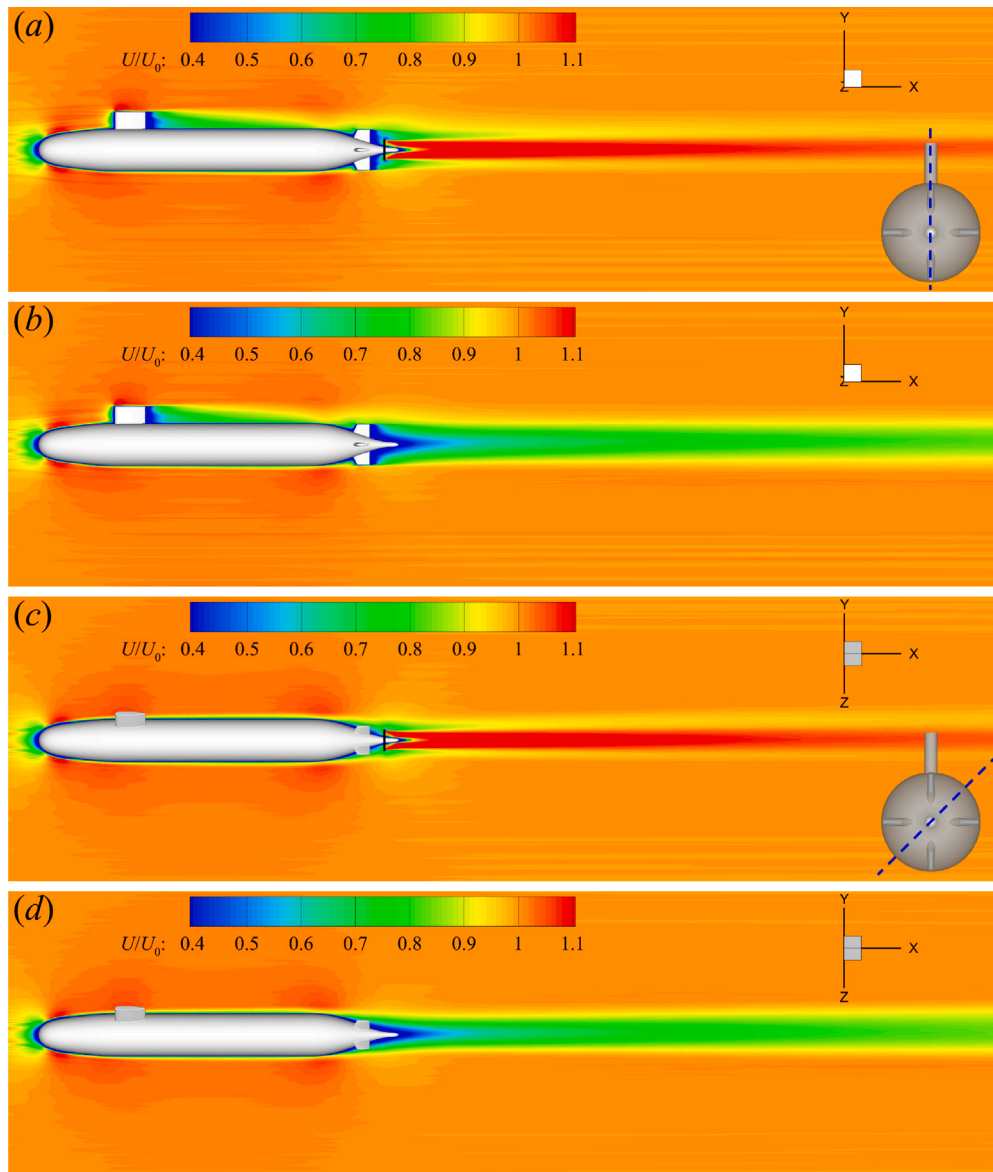
Fig. 4. Time-averaged streamwise velocity at the two-dimensional slice of $z = 0.0$ (a~b) and $y + z = 0.0$ (c~d): (a)(c) Suboff model with AD; (b)(d) Suboff model without AD. In (a) and (c), the bottom right figures show the planes on side view.

$x/L = 0.03$, where the C_p computed in this work is smaller than those in the experiment. As for the C_f in Fig. 3(f), the agreement is acceptable considering the relatively coarse grid employed in this work. The major difference lies near the aft part of the body with an underpredicted C_f, which is probably due to the effect of the pressure gradient is not modeled in the wall model. The comparison of the C_p and C_f from the WMLES and the WRLES of Posa and Balaras (2020) was done in our previous work (Zhou et al., 2021), with a similar case setup.

Figs. 4 and 5 compare the contours of time-averaged streamwise velocity U and pressure P at two slices along the centerline of the hull with different azimuthal angles, one located at the $z = 0.0$ plane passing through the sail and one fin (a~b), the other one located at the $y + z = 0.0$ plane with inclined 45° to avoid passing through the appendages (c~d). The black line behind the fins represents the actuator disk. As seen in (b) and (d) of Figs. 4 and 5, the effect of the appendage is apparent, i.e., a low speed wake in its downstream and a pressure rise in its upstream. The low-speed wake downstream the sail in Fig. 4(b) is observed extending along the hull surface, making the wake downstream the Suboff asymmetric. Comparing Fig. 4(a) and (b), the actuator disk accelerates the downstream flow to generate a

long-extended high-speed jet region. As for the comparison shown in Fig. 5(a) and (b), the actuator disk causes a pressure jump in the wake region downstream of the fins, while the extent of the high-pressure region downstream the disk becomes larger, beyond which it recovers quickly to the ambient pressure.

Then in Fig. 6 we examine the flow field on the two-dimensional slices located at different streamwise locations. As seen, the flows are similar for cases with/without the AD propeller, for $x/D = 1$ to 7 (i.e., the fore and middle part of the hull). At $x/D = 8$, the flow experiences significant deceleration while passing through the stern, and the AD propeller confines slightly the size of the low-speed wake region in Fig. 6(a) when compared with Fig. 6(b). In the near wake of the Suboff without the AD propeller at $x/D = 9, 10$ (Fig. 6 b), the velocity-deficit has a diamond shape and is distributed asymmetrically in the upper and lower parts of the wake due to the cross-shape stern rudders and the sail. The AD propeller introduces a high-speed round jet along the centerline and accelerates the recovery of the velocity in the velocity-deficit regions.
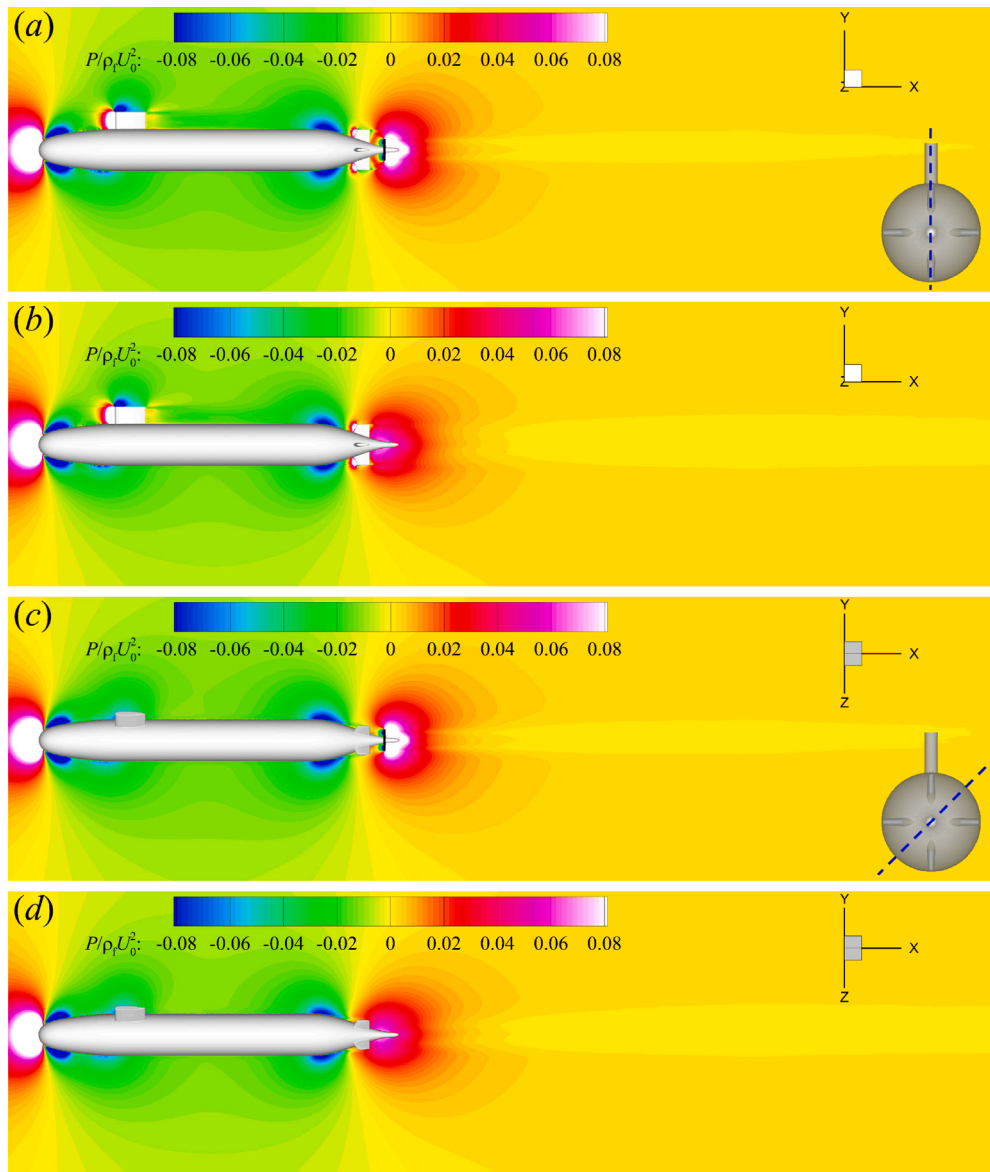
Fig. 5. Time-averaged pressure distribution at the two-dimensional slice of $z = 0.0$ (a~b) and $y + z = 0.0$ (c~d): (a)(c) Suboff with AD propeller; (b)(d) Suboff without AD propeller.

4.2. Wake characteristics

After showing the global flow field, in this section we examine the effect of the AD propeller on the wake characteristics of the Suboff, especially in the far wake region. Figs. 7 and 8 compare the transverse profiles of the time-averaged streamwise velocity, the pressure and the streamwise component of Reynolds stresses on the slices defined by $z = 0.0$ and $y + z = 0.0$ (45° inclined), respectively.

As seen, the three flow quantities all vary significantly in the near wake (until $x/D = 12$, i.e., $3.4D$ from the stern) in the transverse directions. In Fig. 7(a), the transverse profile of the velocity deficit for the case without the AD propeller is of "V" shape, that the maximum velocity deficit is approximately located along the centerline. The AD propeller changes the velocity distribution in the near wake (e.g., $x/D = 8.7, 9.0, 10$), where three local minima and two local maxima are observed, reflecting the three-layer wake–jet–wake flow structures. At further downstream locations, the streamwise velocity distribution from the case with the AD propeller become less complex, with an inner jet surrounded by a wake. As for the pressure shown in Fig. 7(b), the peak value located at the centerline is observed in the near wake, with an abrupt decrease of magnitude from $x/D = $

8.7 to 10. The AD propeller is observed to increase the magnitude of pressure, especially at $x/D = 8.7$. For the streamwise component of Reynolds stress ($u'u'$) shown in Fig. 7(c), fairly complex variations in the transverse direction are observed at near wake locations, i.e., $x/D \leq 11$, as a result of the complex interplay between the wakes from the hull, fin, sail, and the AD propeller.

For the comparison in the $y + z = 0.0$ plane, the plotted profiles of the flow statistics are similar to those in the $z = 0.0$ plane, but showing a smaller wake width as it is not located in the direct downstream of the sail and the stern rudders. In Fig. 8(a), the velocity deficit from the case without the AD propeller is featured by a bell shape close to the Gaussian distribution at all streamwise locations, while the case with the AD propeller has a more complex shape consisting of a jet region and two velocity-deficit regions. For the pressure distribution shown in Fig. 8(b), the transverse variations in the $y + z = 0.0$ plane are similar to those in the $z = 0.0$ plane for the considered streamwise locations. For the streamwise component of Reynolds stresses shown in Fig. 8(c), a higher magnitude is observed in the upper region ($y/D > 0$), being similar for both cases with and without the AD propeller. According to the comparisons on both slices shown in Figs. 7 and 8, the effect of the AD propeller in the near wake is on the generation of the jet and
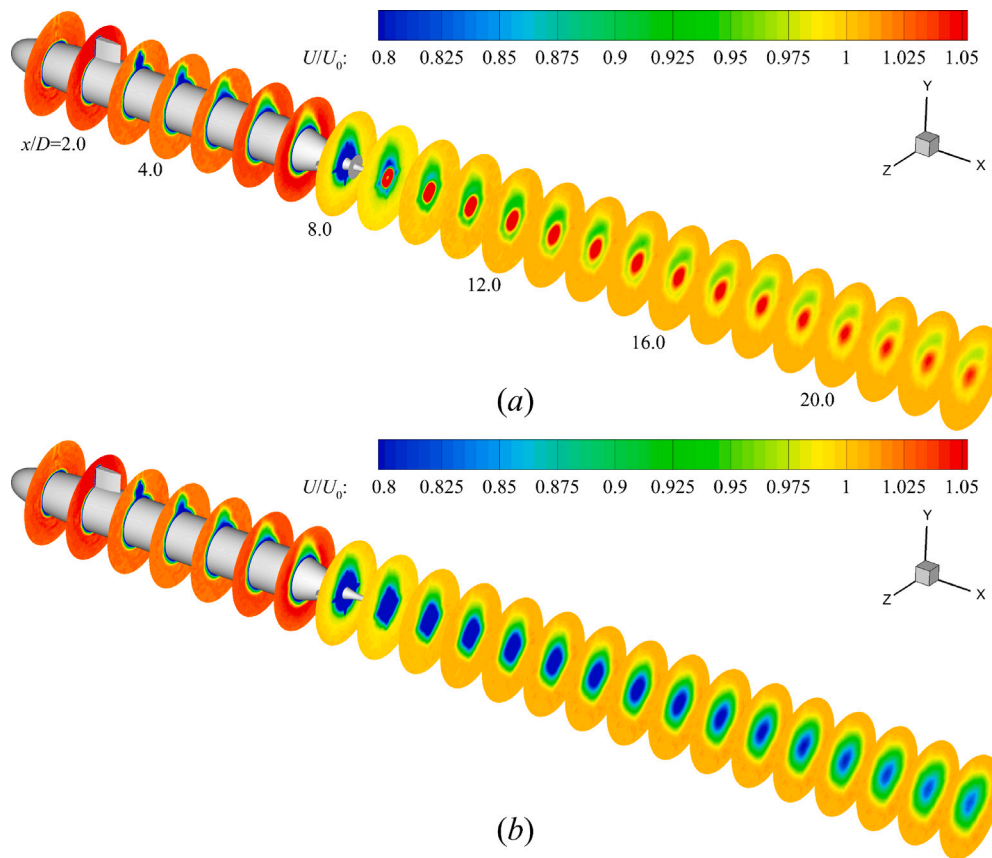
Fig. 6. Time-averaged streamwise velocity U/U_0 at the two-dimensional slices with $x/D = 1.0 \sim 23.0$: (a) Suboff with AD propeller; (b) Suboff without AD propeller.
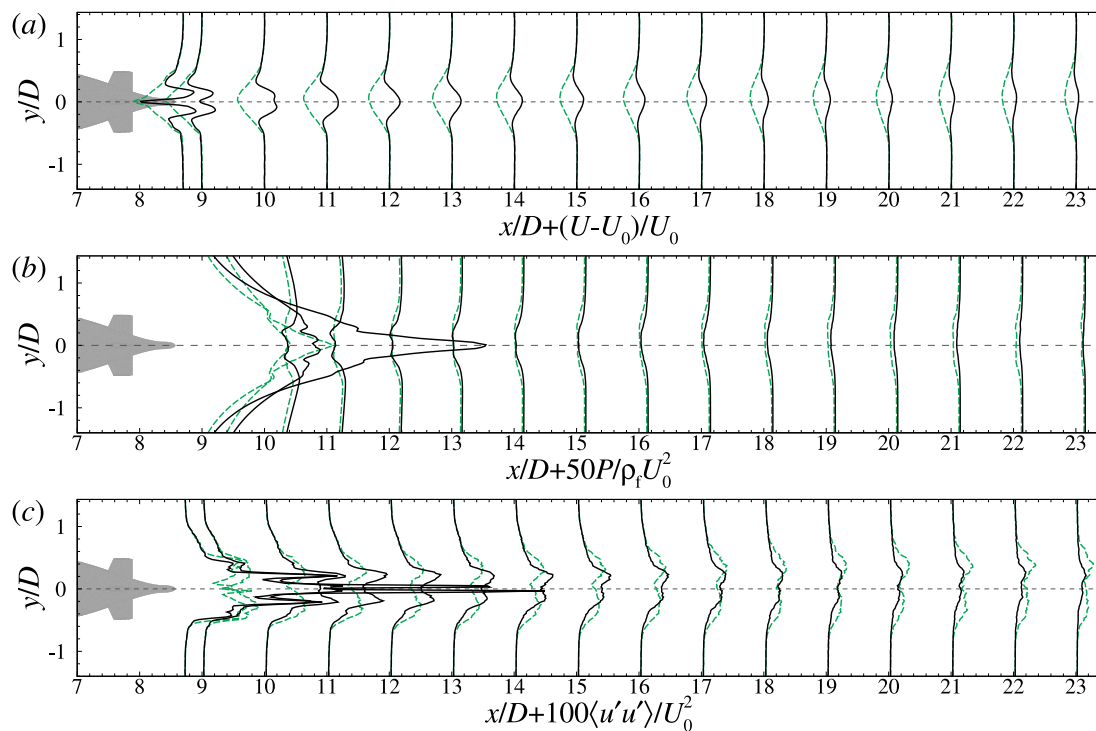

Fig. 7. Comparison of the transverse profiles of (a) time-averaged streamwise velocity, (b) time-averaged pressure, and (c) the streamwise component of Reynolds stresses in the $z = 0.0$ plane, where the solid and dashed lines denote the results of simulations with and without AD propeller, respectively, overlaid on the corresponding contour from the case with the AD propeller. The profiles are located at $x/D = 8.7$, and $x/D = 9.0 \sim 23.0$ with increment of 1, respectively.
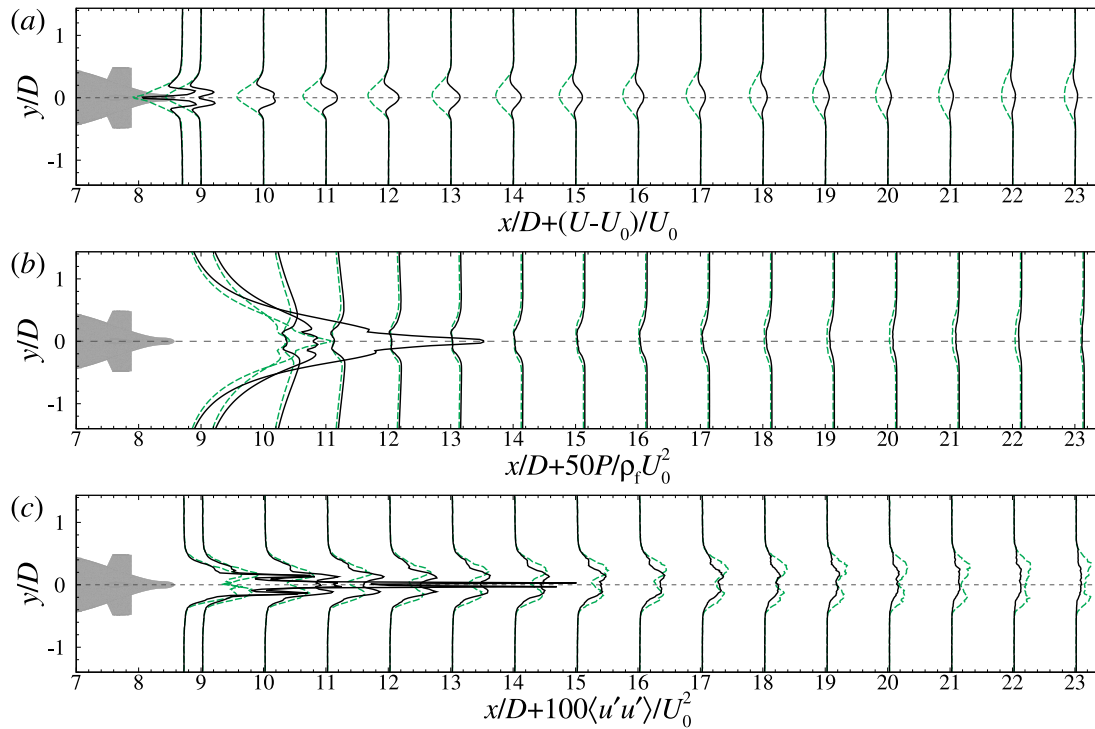
Fig. 8. Comparison of transverse profiles of (a) time-averaged streamwise velocity, (b) time-averaged pressure, and (c) the streamwise component of Reynolds stresses in the $y + z = 0.0$ plane, where the solid and dashed lines denote the results from simulation with and without AD propeller, respectively, overlaid on the corresponding contour from the case with the AD propeller. The profiles are located at $x/D = 8.7$, and $x/D = 9.0 \sim 23.0$ with increment of 1, respectively.

the increase of pressure. Its effect in the far wake will be systematically examined in the following.

In Fig. 9, we divide the wake into two regions, i.e., $9 \le x/D \le 23$ and $24 \le x/D \le 60$, and compare the transverse profiles of different quantities from the two cases, focusing on how the AD affects the wake in a quantitative way. We first examine the time-averaged streamwise velocity profiles in Figs. 9(a,b). It is seen that the transverse width affected by the AD propeller (which is defined as the region where the velocity profile from the case with and without the AD propeller exhibit significant difference) changes as traveling in the downstream direction. At $x/D = 9$, the influence of the AD is concentrated in the range of $-0.3 < y/D < 0.3$, slightly larger than the diameter of the disk, and the velocity profiles from the cases with and without the AD propeller approximately collapse with each other in the rest of the region. This AD-influenced region expands as moving downstream, with its upper boundary from $y/D \approx 0.3$ at $x/D = 9$ and $y/D \approx 0.6$ at $x/D = 15$, to $y/D \approx 1$ at $x/D = 60$, and its lower boundary $y/D \approx -0.3$ at $x/D = 9$ and $y/D \approx -0.5$ at $x/D = 15$, to $y/D \approx -0.8$ at $x/D = 60$, respectively. It is noticed that the upper boundary of this AD-influenced region moves outward in a faster way when compared with the lower boundary, which is consistent with the faster movement of the upper boundary of wake, because of the higher magnitude of velocity deficit in the upper region.

While expanding outward when mixing with the surrounding flow, the velocity-deficit region from the case with the AD propeller also expands inward and interacts with the jet caused by the AD propeller. This inward expansion of the velocity-deficit region can be marked by the intersection point of the velocity profile with the vertical profile located at $U/U_0 = 1$. It is observed that the intersection point gradually moves outward as traveling downstream, from $y/D \approx 0.25$ at $x/D = 12$ to $y/D \approx 0.5$ at $x/D = 60$ for the upper one, and $y/D \approx -0.25$ at $x/D = 12$ to $y/D \approx -0.7$ at $x/D = 60$ for the lower one, respectively. Although the momentum mixing is stronger around the upper intersection point, the AD propeller jet expands at a lower rate in the upper region (as

indicated by the position of the upper intersection point) because of the confinement introduced by the upper velocity-deficit region. This phenomenon is in contrast with the expansion of a jet (or wake) in freestream, for which stronger momentum mixing across the boundary is associated with a higher expansion rate.

In the near wake, other than the interaction of the jet with the velocity-deficit region surrounding it from the outward, the jet also interacts with the velocity-deficit region along the centerline. This interaction is evidenced at $x/D = 12$ as shown in Figs. 9(a), where the maximum velocity deficit is observed close to the centerline and two peaks for the jet appear in the upper and lower regions. It is also noticed that velocity magnitude at the upper peak is lower, where the magnitude of velocity deficit is higher due to the effect of the sail. At further downstream locations, the velocity profile from the case with the AD propeller is featured by one peak for the maximum velocity, which moves slowly upwards from the centerline to a location above it (see Fig. 10(b)).

The effects of the AD propeller on the Reynolds normal stresses are examined in Figs. 9(c–h). It is seen that the AD propeller affects the magnitude as well as the distribution of Reynolds stresses. At $x/D = 9$, the high-magnitude Reynolds stresses from the case with the AD propeller is mainly distributed in three regions, i.e., the $-0.3 < y/D < -0.1$, $-0.1 < y/D < 0.1$ and $0.1 < y/D < 0.3$ regions, respectively, which correspond to the interaction of the jet with the velocity-deficit regions from the inner and outer sides. For the case without the AD propeller, on the other hand, the regions with high-magnitude Reynolds stresses are located above and below the centerline, respectively, with the magnitudes of the Reynolds stresses higher in the upper region at $x/D = 12.0$ and further downstream locations. Compared with the results from the case without the AD propeller, the maximal magnitudes of the Reynolds stresses from the case with the AD propeller are higher at near wake locations (e.g., $x/D = 9.0, 12$) but are lower at far wake locations (e.g., $x/D = 21$ and further).
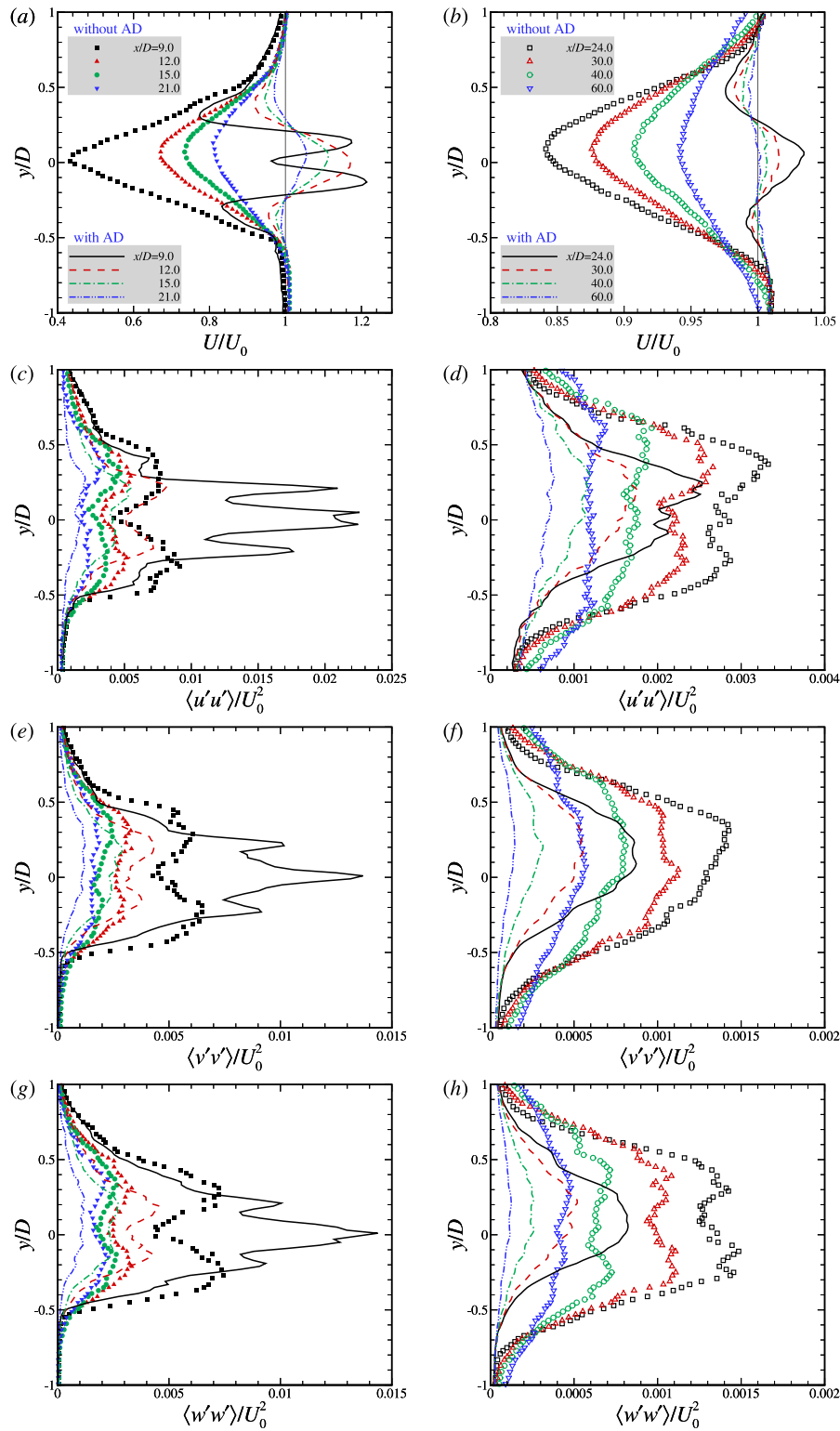
Fig. 9. Comparison of profiles of (a)(b) time-averaged streamwise velocity and velocity fluctuations at (c)(d) streamwise, (e)(f) vertical, and (g)(h) spanwise direction in the $z = 0.0$ plane, where the lines and symbols denote the results from the Suboff model with and without AD propeller. The profiles are located at $x/D = 9.0$, 12.0, 15.0, 21.0, 24.0, 30.0, 40.0 and 60.0, respectively.

After showing the effect of the AD propeller, in the following, we examine the existence of self-similarity in the wake of the Suboff model with and without the AD propeller. If the self-similarity exists, the velocity profiles at different downstream locations can collapse

with each other when normalized with proper velocity and length scales (Pope, 2000). For the jet, the length scale is defined as its width d_{jet}, the distance between the upper and lower transition points where $U/U_0 = 1$, and its velocity scale is defined as the streamwise velocity
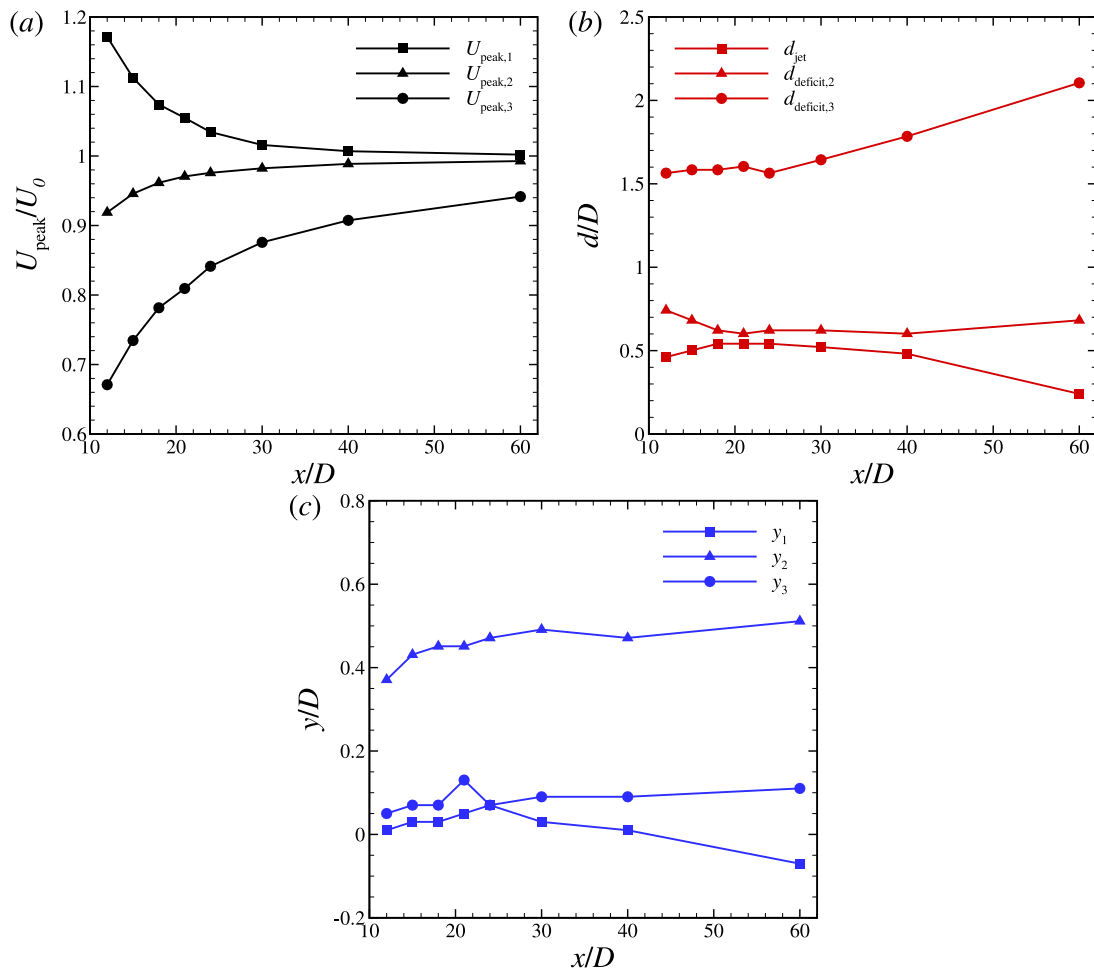
Fig. 10. The variations of parameters for scaling profiles of time-averaged streamwise velocity in the $z = 0.0$ plane: (a) Peak velocity at the region of jet and velocity deficit; (b) vertical location of the peak velocity; (c) the width of scaling region.

$U_{\mathrm{peak},1}$ at the jet center y_1. For the velocity-deficit region above the jet, the length scale $d_{\mathrm{deficit},2}$ is defined as the distance between the upper transition point (where $U/U_0 = 1$) and the top boundary of the wake (where $U/U_0 \approx 1$), and the velocity scale $U_{\mathrm{peak},2}$ is defined as the magnitude of the minimum velocity at the upper wake center y_2. For the wake of the Suboff model without the AD propeller, the length scale is defined as the distance between the upper and lower boundaries (where $U/U_0 \approx 1$), and the velocity scale $U_{\mathrm{peak},3}$ is defined as the magnitude of the minimum velocity at the wake center y_3.

In Fig. 10, the downstream variations of the obtained characteristic length and velocity scales and wake centers are plotted. It is seen in Fig. 10(a) that the magnitude of the velocity scale decreases for the jet, while increases for the velocity-deficit region as one travels downstream. As shown in Fig. 10(b), the jet width d_{jet} increases with x in the near wake, while gradually decreases with x at further downstream locations. The width of the upper velocity-deficit region $d_{\mathrm{deficit},2}$ for the case with the AD propeller, on the other hand, decreases in the near wake and remains approximately at the same level at further downstream locations. The wake width $d_{\mathrm{deficit},3}$ for the case without the AD propeller in general increases with x, but at a very low rate in the near wake. As for the wake centers shown in Fig. 10(c). the centers for the velocity-deficit region, i.e., y_2 and y_3 in general move upward as one travels in the downstream direction. The jet center y_1, on the other hand, moves upward in the near wake, while gradually moves downward at further downstream locations.

With the obtained velocity and length scales, the self-similarity of the wake of the Suboff model is examined in Fig. 11. In Fig. 11(a)

for the jet, An acceptable overlap is observed, although the velocity profiles are in general skewed to the negative y side at different downstream locations, as its upper boundary is confined by the upper velocity-deficit region. The velocity profiles for the velocity-deficit region located above the jet (as shown in Fig. 11(b)) are skewed to the positive y side, with not bad overlaps among profiles from different downstream locations. The self-similarity of the wake of the Suboff model without the AD propeller is examined in Fig. 11(c). One can observe that the velocity profiles are skewed to the positive y side in the near wake, while are close to symmetry at further downstream locations ($x/D > 24.0$), with overlapped profiles in the near wake and the far wake, respectively.

At last, we examine the spectral characteristics of turbulence in the far wake for cases with and without the AD propeller. Fig. 12 plots the pre-multiplied power spectral density (PSD) of the streamwise, vertical and spanwise velocity fluctuations at $y/D = 0.0, 0.258, 0.5$ for downstream locations at $x/D = 20.0, 40.0$, and 60.0. The PSD is defined as $\Phi = \langle \hat{u}(f)\hat{u}^*(f) \rangle / \Delta f$, where $\hat{u}(f)$ denotes a windowed Fourier transform of the fluctuating velocity, and $\Delta f = 2\pi/T$, T denotes the length of temporal signals. In semi-log coordinate, the area enclosed by the curve $\int f \Phi d(\ln f) = \int \Phi df$ then represents the corresponding turbulent kinetic energy. Comparing the pre-multiplied PSD at the three downstream locations, it is seen that the maximum value decreases as traveling downstream due to the decay of turbulence. Along the centerline, it is seen in Fig. 12(a, b, c) that the AD propeller decreases the level of the PSD at low frequencies for all the velocity components
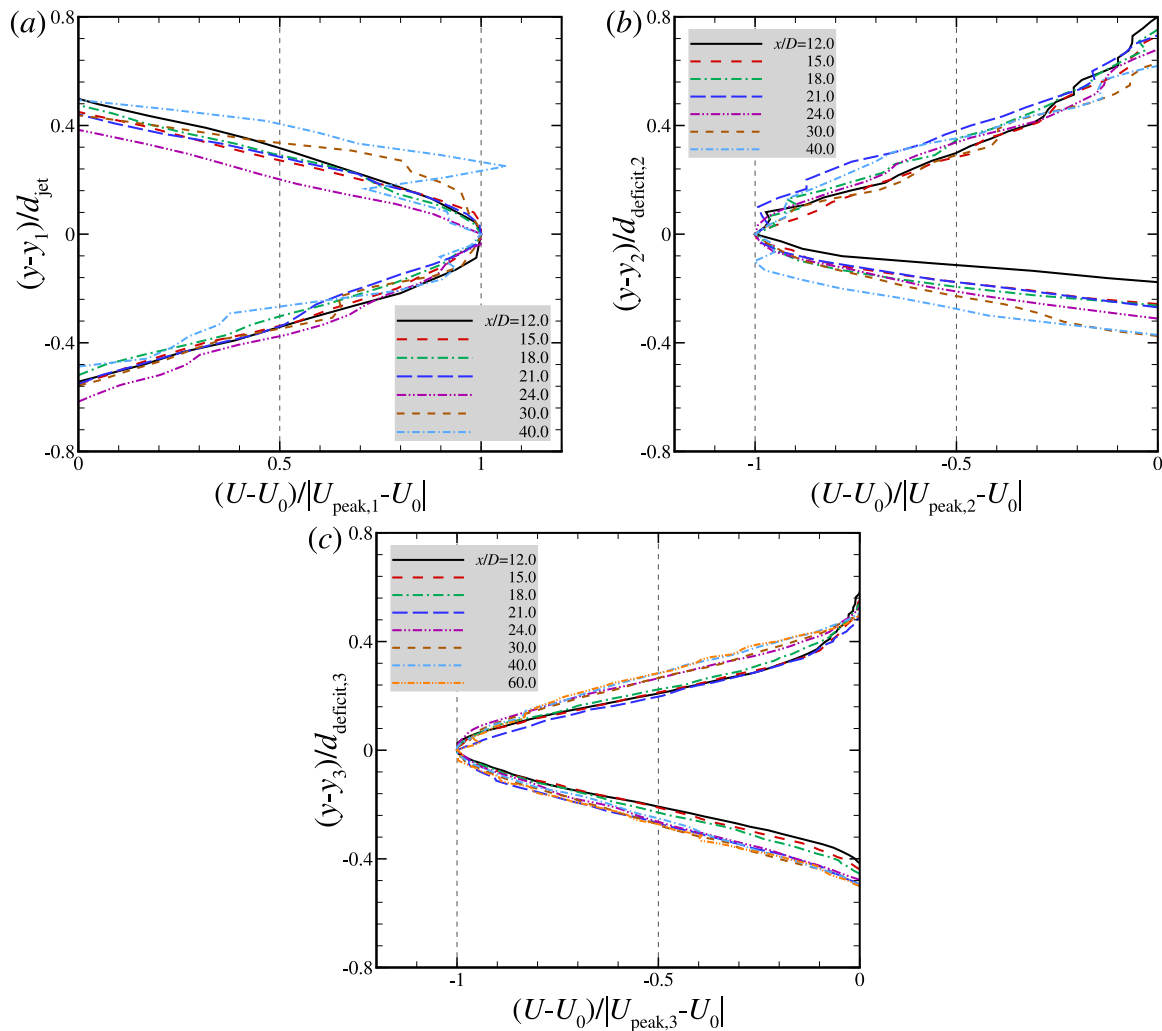
Fig. 11. The scaling profiles of time-averaged streamwise velocity in the $z = 0.0$ plane: (a) the jet region; (b) the deficit region in the positive y-axis of Suboff with AD propeller; (c) the deficit region of Suboff without AD propeller.

at $x/D = 20$, while increases it at high frequencies. At the far wake locations, i.e., $x/D = 40$ and 60, the AD propeller decreases the levels of the PSD at almost all frequencies. At $y/D = 0.258$ shown in Fig. 12(d,e,f), the effect of the AD propeller on the PSD is similar to that at $y/D = 0.0$, but the levels of the PSD at low frequencies become higher, which demonstrate that the momentum mixing near the edge of AD propeller is stronger. As moving upward further at $y/D = 0.5$ shown in Fig. 12 (g,h,i), the levels of the PSD are decreased at almost all frequencies because of the AD propeller. Detailed space–time correlation study (He et al., 2017) can be conducted in further studies to reveal the mechanism of such downstream variations of the turbulence fluctuations.

5. Conclusions

In this work, we investigated the wake characteristics of the DARPA Suboff submarine model in both towed and self-propelled conditions using large-eddy simulation with the hull and appendages geometrically resolved using the curvilinear immersed boundary method and the propeller parameterized using the actuator disk (AD) model. Two cases with/without the AD propeller were simulated.

The simulation results show that the AD propeller has a profound effect on both the near wake and the far wake, with its effects on the pressure and friction coefficients on the Suboff constrained in its

nearby region. Without the AD propeller, the wake of the Suboff model is featured by a single velocity-deficit region of a diamond-like shape, due to the combined effects of the sail and the fins. Introducing the AD propeller adds a round jet along the centerline. In the very near wake, the inner part of the round jet is occupied by the velocity-deficit region due to the hull, which fast decays. At further downstream locations, the dominant interaction occurs between the jet and the surrounding velocity-deficit region, especially for the upper part in the wake of the sail.

As for the turbulence statistics, in the near wake (before the disappearance of the inner velocity-deficit region, e.g., $x/D = 9.0$) the AD propeller increases the number of peaks of the Reynolds stresses and the magnitudes of the peaks. As one moves further downstream, the numbers of the peaks from the cases with and without the AD propeller are the same. With the AD propeller, the peak values of the Reynolds stresses are located closer to the centerline, with their magnitudes being higher at the near wake locations (e.g., $x/D = 9, 12$) but lower at the far wake locations (e.g. $x/D = 21, 24$ and further,) when compared with the case without.

The self-similarity is examined for the transverse profiles of the streamwise velocity. Different from a single wake, for which its downstream evolution is only affected by the momentum mixing with the ambient flow, the momentum mixing for the wake from the Suboff
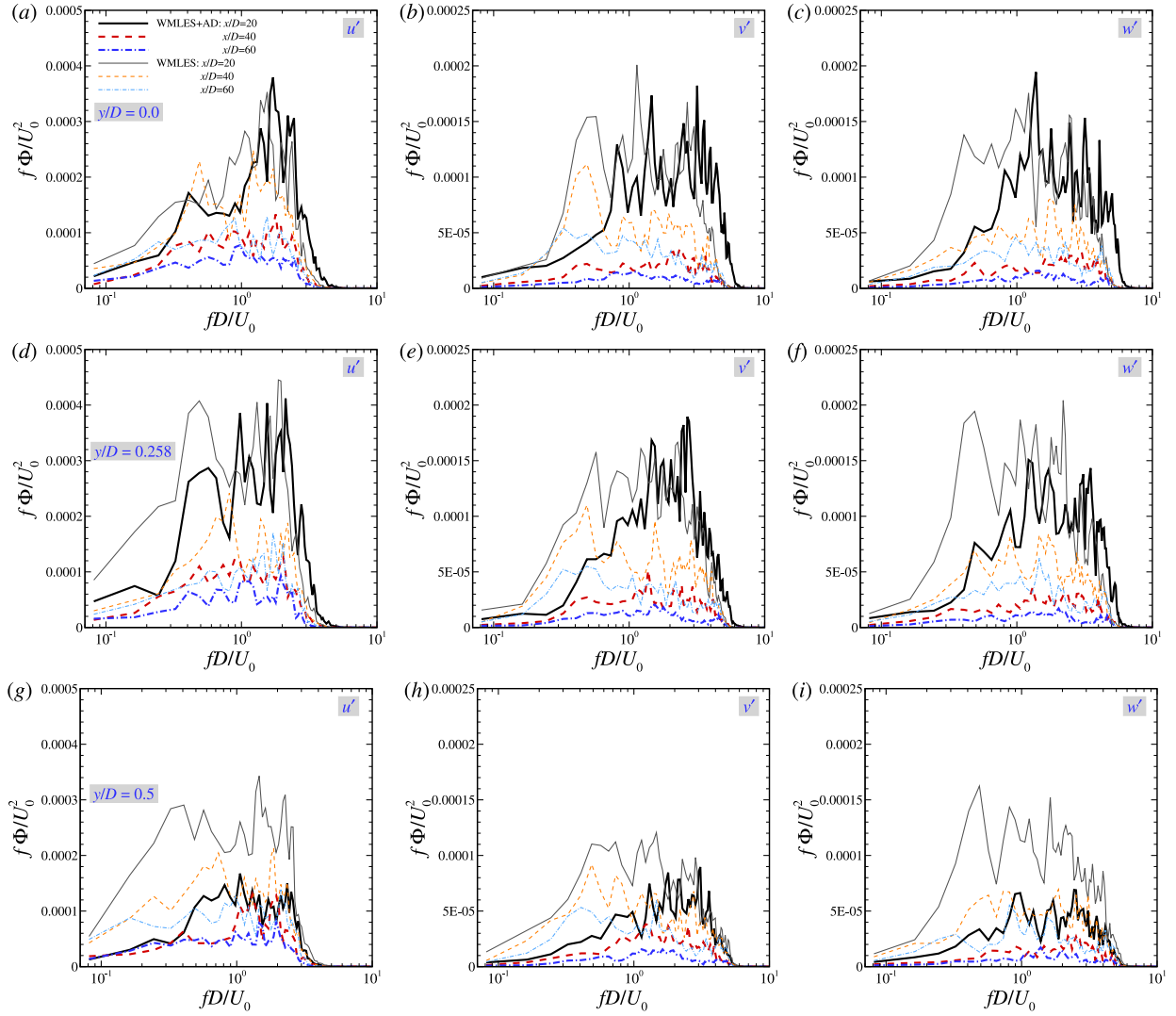
Fig. 12. Pre-multiplied power spectral density of one-dimensional spectra of (a) streamwise, (b) vertical and (c) spanwise velocity fluctuations at streamwise locations $x/D = 20.0$, 40.0, and 60.0 along the line of $z/D = 0.0$, $y/D = 0.0, 0.258, 0.5$ for Suboff with and without AD propeller. The horizontal and vertical axes are normalized with U_0/D and U_0^2, respectively.

Table B.3
Details of the coarse grid and fine grid employed in the grid refinement study, which include the grid spacing (Δh) and the number of grids (N) at different locations. For the grid spacing, "u" denotes the uniform grid, "r" and "l" denote the non-uniform grid defined using the tanh function, with the smallest grid cell on the right and left side, respectively.

$x/D \in$	$[-2.6, -0.4]$	$[-0.4, 2.0]$	$[2.0, 6.0]$	$[6.0, 16.0]$	$[16.0, 23.2]$
N	35	80	90	500	135
$\Delta h/D$	0.03 (r)	0.03 (u)	0.03 (l) 0.02 (r)	0.02 (u)	0.02 (l)
$y/D \in$	$[-4.3, -1.2]$		$[-1.2, 1.2]$		$[1.2, 4.3]$
N	80/120		200/400		80/120
$\Delta h/D$	0.012/0.006 (r)		0.012/0.006 (u)		0.012/0.006 (l)
$z/D \in$	$[-4.3, -1.2]$		$[-1.2, 1.2]$		$[1.2, 4.3]$
N	80/120		200/400		80/120
$\Delta h/D$	0.012/0.006 (r)		0.012/0.006 (u)		0.012/0.006 (l)

with the AD propeller happens across the boundary between the jet and the velocity-deficit regions, and the boundary between the whole wake and the ambient flow. Acceptable overlaps are observed for the jet and velocity-deficit regions for certain ranges of downstream locations.

At last, the power spectra of velocity fluctuations are examined. The results show that the effects of the AD propeller are different at different upper locations away from the centerline. At locations near the centerline (e.g., $y/D = 0.0, 0.258$, with the latter one for the upper
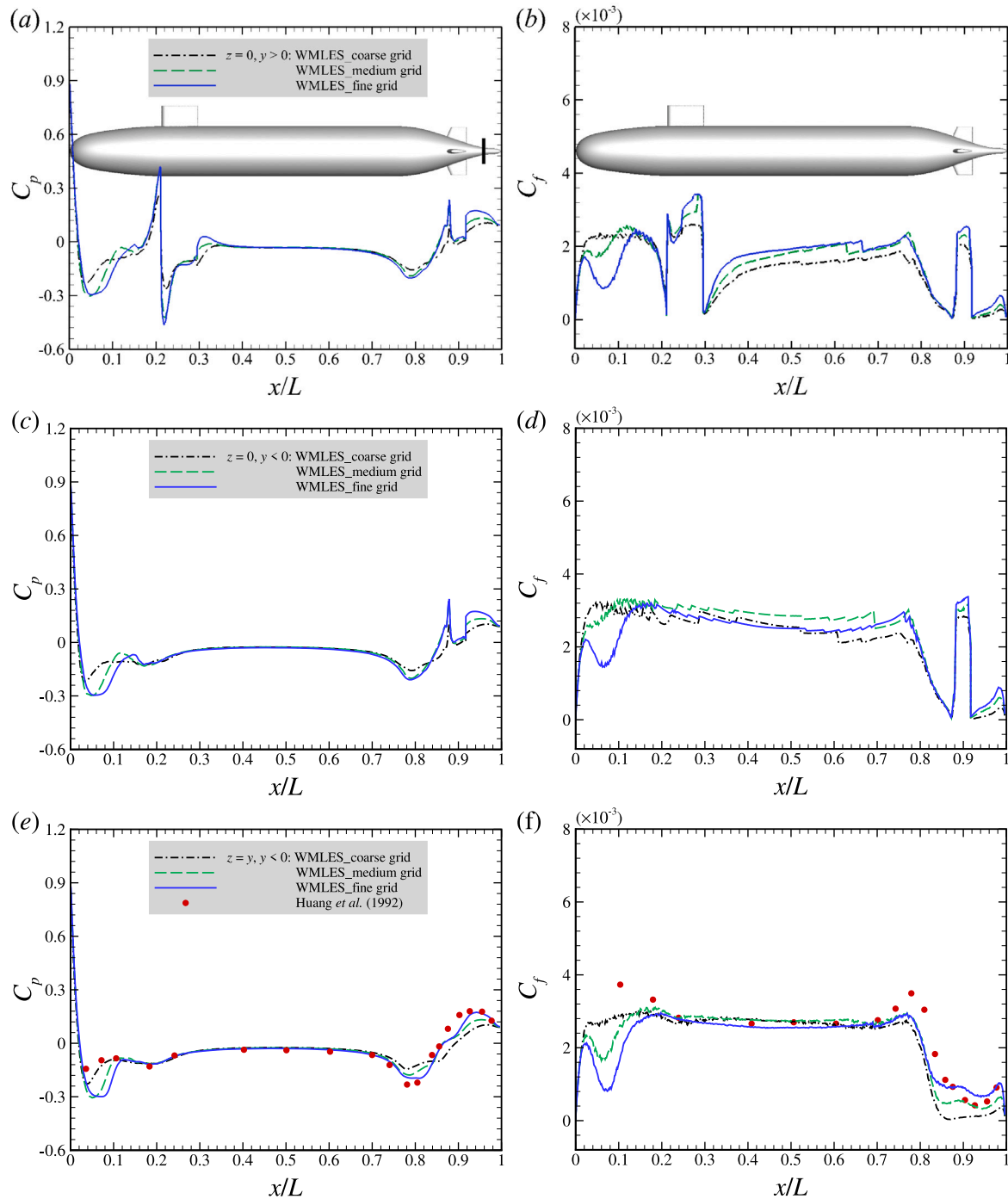
Fig. B.13. Comparisons of the pressure coefficient C_p and skin-friction coefficient C_f obtained from the simulations on the coarse, medium and fine grids, and the results from the experiment of Huang et al. (1994) for (a~b) $z = 0, y > 0$, (c~d) $z = 0, y < 0$ and (e~f) $z = y, y < 0$.

tip of the AD propeller), the AD propeller increases the levels of the PSD at high frequencies at $x/D = 20$. At locations away from the centerline (e.g., $y/D = 0.5$), on the other hand, the AD propeller decreases the levels of the PSD at almost all frequencies for the considered downstream locations.

This work has been focused on two cruising conditions. Other cruising conditions, such as acceleration, deceleration, and turning, will be considered in the future work. It is still challenging to simulate flows over Suboff-like bodies using wall-modeled LES. Further work on developing more accurate LES models for such flows is surely needed.
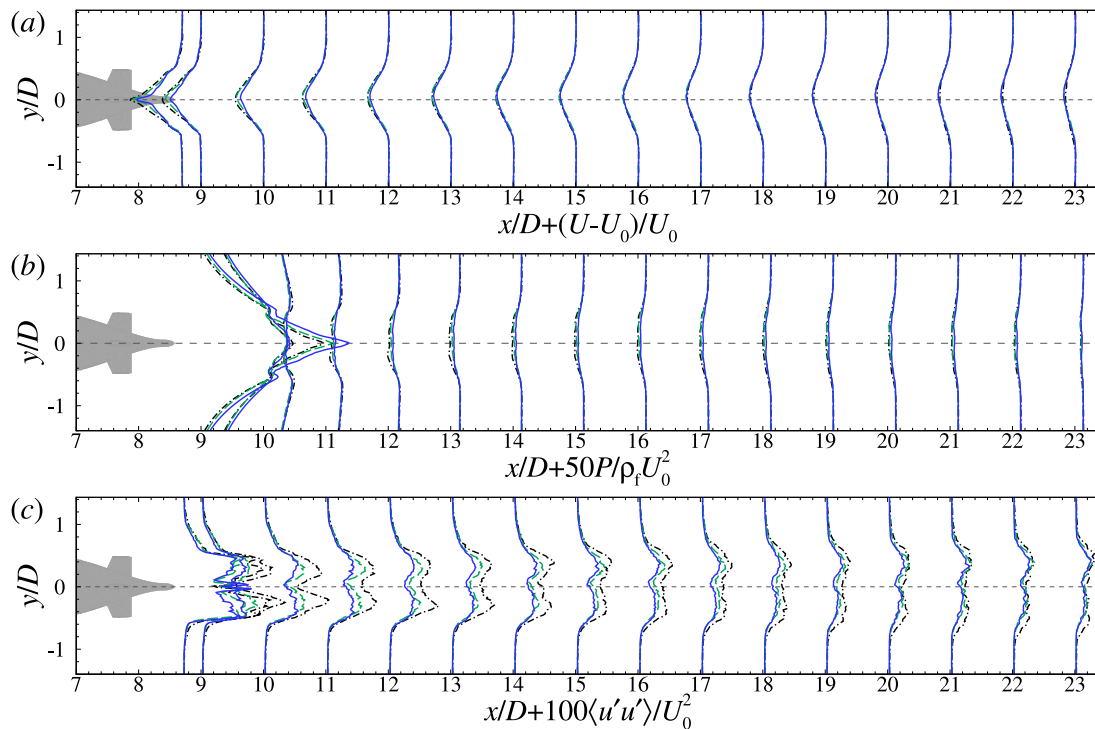
Fig. B.14. Comparison of the transverse profiles obtained from the simulations on the coarse (dash-dot lines), medium (dashed lines) and fine (solid lines) grids for (a) time-averaged streamwise velocity, (b) time-averaged pressure, and (c) the streamwise component of Reynolds stresses in the $z = 0.0$ plane.

CRediT authorship contribution statement

Zhideng Zhou: Conceptualization, Methodology, Investigation, Writing – original draft, Visualization. **Zhaobin Li:** Software, Validation, Writing – review & editing. **Xiaolei Yang:** Conceptualization, Writing – original draft, Writing – review & editing, Supervision. **Shizhao Wang:** Writing – review & editing. **Duo Xu:** Writing – review & editing.

Declaration of competing interest

The authors declare that they have no known competing financial interests or personal relationships that could have appeared to influence the work reported in this paper.

Data availability

Data will be made available on request.

Acknowledgments

Appendix A. Computational cost

The simulations were performed on the CAS SunRising-1 platform, CNIC, China, of which each node consists of 32 core HYGON CPU at 2.0 GHz. The simulations of Suboff with and without AD propeller were carried out for about 13.5 flow through times (from $x/D = -2.6$ to $x/D = 23.2$) using 1800 CPU cores, yielding about 140 h (2.52×10^5 CPU hours) and 127 h (2.28×10^5 CPU hours), respectively. The continuous simulations of far wake both require the other 27 h on 1200 CPU cores (3.23×10^4 CPU hours), which covers about 5.5 flow through times (from $x/D = 16.0$ to $x/D = 60.0$).

Appendix B. Grid refinement study and validation

To examine the grid dependence of the simulation results, simulations of the case without a AD propeller are conducted on two additional grids, a coarse grid ($841 \times 361 \times 361$) and a fine grid ($841 \times 621 \times 621$). Table B.3 shows the number of grids and grid spacings in different regions. Compared to the medium grid resolution ($841 \times 501 \times 501$) shown in Table 1, the changes of the grid resolution are located in the region around the Suboff body in y and z directions.

Fig. B.13 compares the pressure and friction coefficients obtained from the WMLES with three grid resolutions. Both the C_p and C_f exhibit good consistency on most parts of the hull surface, especially for the parallel middle body and the stern. The major differences are located near the stern, where the value of C_f and the value of C_p are smaller and larger, respectively, on the fine grid.

Figs. B.14 and B.15 compare the transverse profiles of time-averaged streamwise velocity, pressure and the streamwise component of the Reynolds normal stresses from the WMLES with three grid resolutions on the planes of $z = 0.0$ and $y + z = 0.0$, respectively. At the very near wake locations, e.g., $x/D = 8.7$ and 9.0, some differences between different grid resolutions are observed in the wake statistics, including their maximal magnitudes and the region with high-magnitude streamwise component of the Reynolds normal stresses. At further downstream locations, the flow statistics from different grid resolutions are close with each other, especially between the medium and fine grids.

In the literature, there are not a lot of experimental data available for evaluating the capability of the simulation in predicting the Suboff wake. Fig. B.16 compares the time-averaged streamwise and radial velocity profiles from the present WMLES with the WRLES of Posa and Balaras (2020) and the experiment of Huang et al. (1994) at four streamwise locations near the stern. The profiles employed for comparison are extracted from the plane of $z = y$, $y < 0$ to minimize the influence of the appendages, as the experiment of Huang et al. (1994) was carried out using a bare hull. An overall acceptable agreement is observed, with the observed discrepancies possibly due to (1) the
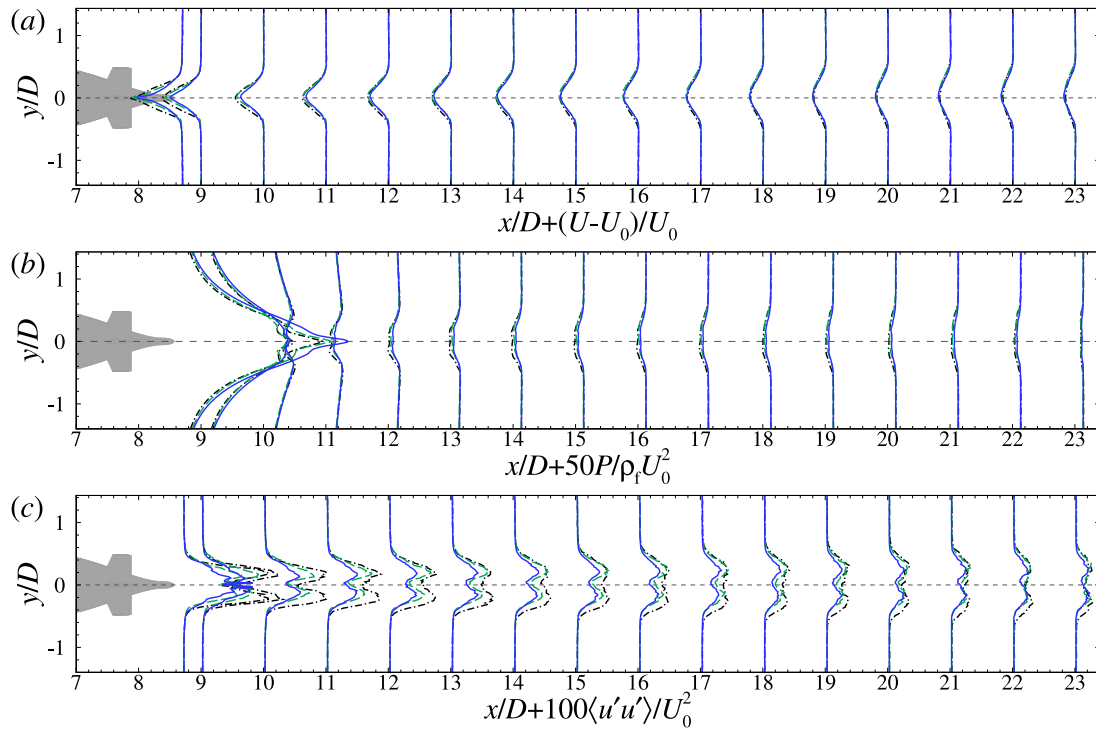
Fig. B.15. Comparison of the transverse profiles obtained from the simulations on the coarse (dash-dot lines), medium (dashed lines) and fine (solid lines) grids for (a) time-averaged streamwise velocity, (b) time-averaged pressure, and (c) the streamwise component of Reynolds stresses in the $y + z = 0.0$ plane.
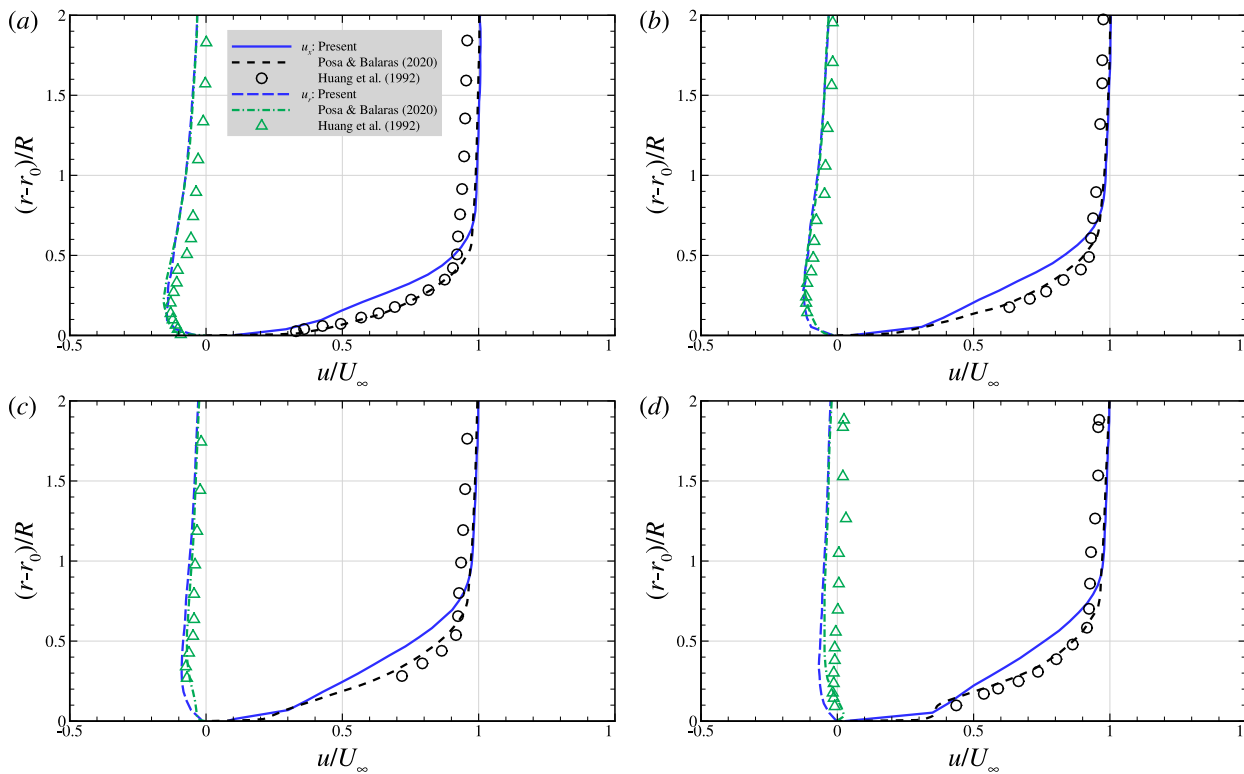

Fig. B.16. Comparisons of time-averaged streamwise (u_x) and radial velocity (u_r) profiles from the present WMLES with the WRLES results of Posa and Balaras (2020) and the experimental results of Huang et al. (1994) at four streamwise locations for (a) $x/L = 0.904$, (b) $x/L = 0.927$, (c) $x/L = 0.956$ and (d) $x/L = 0.978$. Profiles employed for comparison are extracted on the plane between the fins and away from the sail ($z = y, y < 0$) to minimize the effects of the appendages. The medium grid resolution is employed.
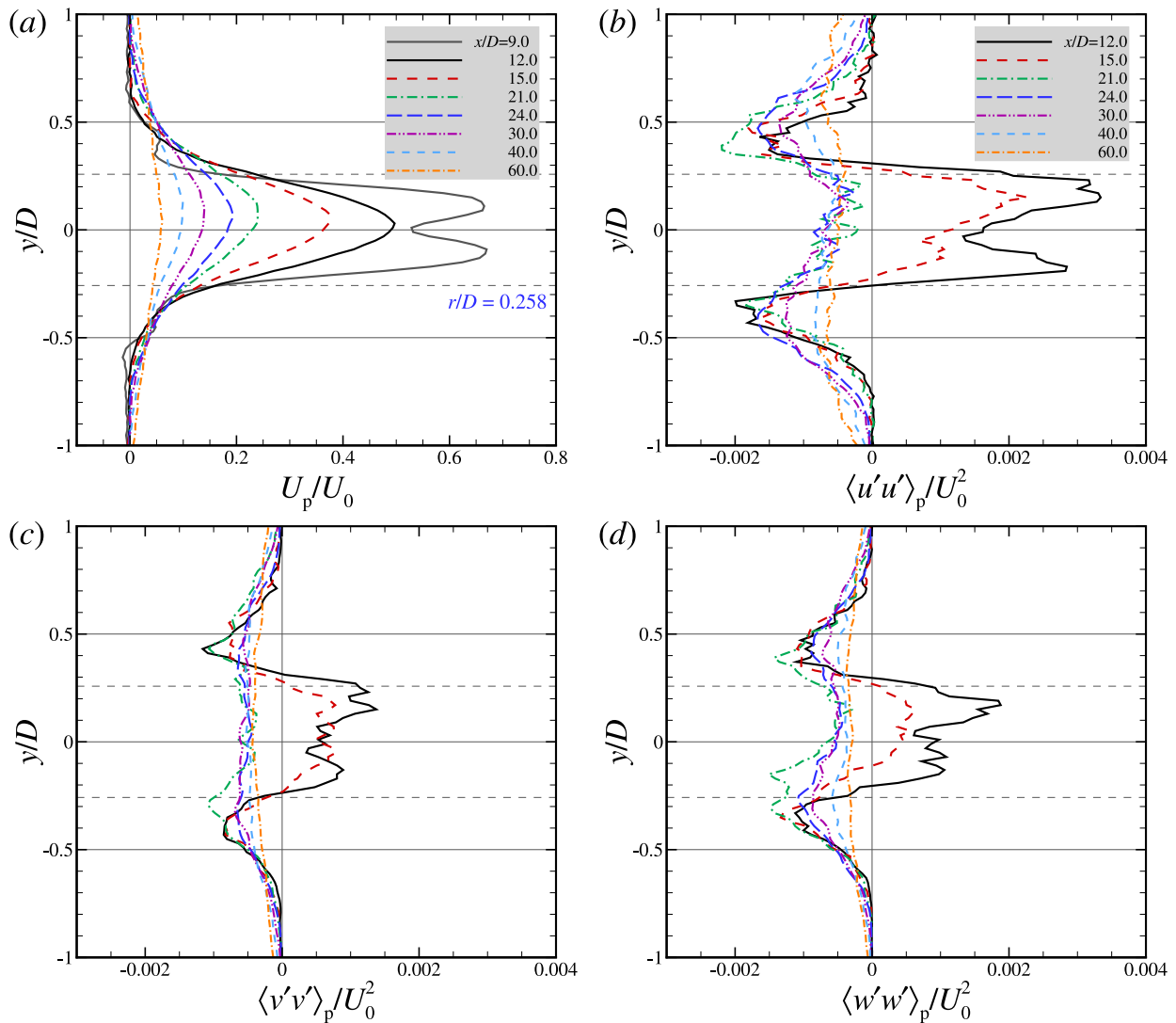
Fig. C.17. Profiles of the flow statistics induced by the AD propeller for (a) the time-averaged streamwise velocity, and (b) the streamwise, (c) the vertical and (d) the spanwise components of the Reynolds normal stresses at different downstream locations in the $z = 0.0$ plane.

relatively coarse grid employed, (2) the incapability of the wall model in to capturing the effect of pressure gradient, and (3) the absence of the numerical trip wire for triggering turbulence transition, which was employed in the work by Posa and Balaras (2020).

Appendix C. Some further analyses of the wake field induced by the AD propeller

In this appendix, the flow statistics induced by the AD propeller are examined by a direct subtraction of the results with and without a propeller, i.e., $f_p = f_{\text{with AD}} - f_{\text{no AD}}$, where f denotes a quantity of the flow statistics.

Fig. C.17 shows the transverse profiles of time-averaged streamwise velocity and the three components of the Reynolds stresses induced by the AD propeller in the $z = 0.0$ plane. It is seen that the center of the AD propeller jet moves upward as one travels downstream, and the maximal increases of Reynolds stresses at $x/D = 9.0$, 12.0 are located in the upper region, as a result of the interaction of the propeller jet with the wake of the sail. One interesting observation is that, the influence of the AD propeller on the Reynolds stresses at $x/D = 12.0$ and 15.0 can be divided into two regions, i.e., the enhanced inner region and the weakened outer region. At further downstream locations where $x/D \geq 21.0$, on the other hand, all the three components of

the Reynolds normal stresses are weakened for the whole wake region. Such wakening effect is caused by the added momentum from the AD propeller, which enhances the mixing of the low-speed and high-speed regions in the wake.

References

Alin, N., Bensow, R.E., Fureby, C., Huuva, T., Svennberg, U., 2010. Current capabilities of DES and LES for submarines at straight course. J. Ship Res. 54, 184–196. http://dx.doi.org/10.5957/jsr.2010.54.3.184.

Balaras, E., Schroeder, S., Posa, A., 2015. Large-eddy simulations of submarine propellers. J. Ship Res. 59 (4), 227–237. http://dx.doi.org/10.5957/JOSR.59.4.150047.

Borazjani, I., Ge, L., Sotiropoulos, F., 2008. Curvilinear immersed boundary method for simulating fluid structure interaction with complex 3D rigid bodies. J. Comput. Phys. 227 (16), 7587–7620. http://dx.doi.org/10.1016/j.jcp.2008.04.028.

Calderer, A., Yang, X., Angelidis, D., Khosronejad, A., Le, T., Kang, S., Gilmanov, A., Ge, L., Borazjani, I., 2015. Virtual flow simulator. Tech. rep., University of Minnesota.

Ge, L., Sotiropoulos, F., 2007. A numerical method for solving the 3D unsteady incompressible Navier-Stokes equations in curvilinear domains with complex immersed boundaries. J. Comput. Phys. 225 (2), 1782–1809. http://dx.doi.org/10.1016/j.jcp.2007.02.017.

Germano, M., Piomelli, U., Moin, P., Cabot, W.H., 1991. A dynamic subgrid-scale eddy viscosity model. Phys. Fluids A 3, 1760. http://dx.doi.org/10.1063/1.857955.

Gilmanov, A., Le, T.B., Sotiropoulos, F., 2015. A numerical approach for simulating fluid structure interaction of flexible thin shells undergoing arbitrarily large deformations in complex domains. J. Comput. Phys. 300, 814–843. http://dx.doi.org/10.1016/j.jcp.2015.08.008.

Gilmanov, A., Sotiropoulos, F., 2005. A hybrid cartesian/immersed boundary method for simulating flows with 3D, geometrically complex, moving bodies. J. Comput. Phys. 207 (2), 457–492. http://dx.doi.org/10.1016/j.jcp.2005.01.020.

Groves, N.C., Huang, T.T., Chang, M.S., 1989. Geometric characteristics of DARPA SUBOFF models. Tech. rep., DTRC/SHD-1298-01. David Taylor Research Center, Bethesda, MD.

He, G.W., Jin, G.D., Yang, Y., 2017. Space-time correlations and dynamic coupling in turbulent flows. Annu. Rev. Fluid Mech. 49, 51–70. http://dx.doi.org/10.1146/annurev-fluid-010816-060309.

Hickling, C., Balantrapu, N.A., Millican, A., Alexander, W.N., Devenport, W.J., 2019. Turbulence ingestion into a rotor at the rear of an axisymmetric body. In: 25th AIAA/CEAS Aeroacoustics Conference. pp. 20–23. http://dx.doi.org/10.2514/6.2019-2571.

Huang, T., Liu, H.L., Groves, N., Forlini, T., Blanton, J., Gowing, S., 1994. Measurements of flows over an axisymmetric body with various appendages in a wind tunnel: the DARPA SUBOFF experimental program. In: Proceedings of the 19th Symposium on Naval Hydrodynamics. National Academy Press, Seoul, Korea.

Jiménez, J.M., Hultmark, M., Smits, A.J., 2010a. The intermediate wake of a body of revolution at high Reynolds numbers. J. Fluid Mech. 659, 516–539. http://dx.doi.org/10.1017/S0022112010002715.

Jiménez, J.M., Reynolds, R.T., Smits, A.J., 2010b. The effects of fins on the intermediate wake of a submarine model. J. Fluids Eng. 132 (3), 21–27. http://dx.doi.org/10.1115/1.4001010.

Kang, S., Lightbody, A., Hill, C., Sotiropoulos, F., 2011. High-resolution numerical simulation of turbulence in natural waterways. Adv. Water Resour. 34 (1), 98–113. http://dx.doi.org/10.1016/j.advwatres.2010.09.018.

Khosronejad, A., Kang, S., Borazjani, I., Sotiropoulos, F., 2011. Curvilinear immersed boundary method for simulating coupled flow and bed morphodynamic interactions due to sediment transport phenomena. Adv. Water Resour. 34 (7), 829–843. http://dx.doi.org/10.1016/j.advwatres.2011.02.017.

Kumar, P., Mahesh, K., 2017. Large eddy simulation of propeller wake instabilities. J. Fluid Mech. 814, 361–396. http://dx.doi.org/10.1017/jfm.2017.20.

Kumar, P., Mahesh, K., 2018. Large-eddy simulation of flow over an axisymmetric body of revolution. J. Fluid Mech. 853, 537–563. http://dx.doi.org/10.1017/jfm.2018.585.

Le, T.B., Sotiropoulos, F., 2013. Fluid-structure interaction of an aortic heart valve prosthesis driven by an animated anatomic left ventricle. J. Comput. Phys. 244, 41–62. http://dx.doi.org/10.1016/j.jcp.2012.08.036.

Liao, F., Wang, S., Yang, X., He, G., 2020a. A simulation-based actuator surface parameterization for large-eddy simulation of propeller wakes. Ocean Eng. 199, 107023. http://dx.doi.org/10.1016/j.oceaneng.2020.107023.

Liao, F., Yang, X., Wang, S., He, G., 2020b. Grid-dependence study for simulating propeller crashback using large-eddy simulation with immersed boundary method. Ocean Eng. 218, 108211. http://dx.doi.org/10.1016/j.oceaneng.2020.108211.

Liefvendahl, M., Fureby, C., 2017. Grid requirements for LES of ship hydrodynamics in model and full scale. Ocean Eng. 143, 259–268. http://dx.doi.org/10.1016/j.oceaneng.2017.07.055.

Liu, L., Chen, M., Yu, J., Zhang, Z., Wang, X., 2021a. Full-scale simulation of self-propulsion for a free-running submarine. Phys. Fluids 33 (4), 047103.

Liu, Y., Zhou, Z., Zhu, L., Wang, S., 2021b. Numerical investigation of flows around an axisymmetric body of revolution by using Reynolds-stress model based hybrid Reynolds-averaged Navier–Stokes/large eddy simulation. Phys. Fluids 33, 085115. http://dx.doi.org/10.1063/5.0058016.

Mann, J., 1998. Wind field simulation. Probab. Eng. Mech. 13 (4), 269–282. http://dx.doi.org/10.1016/S0266-8920(97)00036-2.

Özden, M.C., Gürkan, A.Y., Özden, Y.A., Canyurt, T.G., Korkut, E., 2016. Underwater radiated noise prediction for a submarine propeller in different flow conditions. Ocean Eng. 126, 488–500. http://dx.doi.org/10.1016/j.oceaneng.2016.06.012.

Pope, S.B., 2000. Turbulent Flows. Cambridge University Press.

Posa, A., Balaras, E., 2016. A numerical investigation of the wake of an axisymmetric body with appendages. J. Fluid Mech. 792, 470–498. http://dx.doi.org/10.1017/jfm.2016.47.

Posa, A., Balaras, E., 2018. Large-eddy simulations of a notional submarine in towed and self-propelled configurations. Comput. & Fluids 165, 116–126. http://dx.doi.org/10.1016/j.compfluid.2018.01.013.

Posa, A., Balaras, E., 2020. A numerical investigation about the effects of Reynolds number on the flow around an appended axisymmetric body of revolution. J. Fluid Mech. 884, http://dx.doi.org/10.1017/jfm.2019.961.

Posa, A., Broglia, R., 2022. Development of the wake shed by a system composed of a propeller and a rudder at incidence. Int. J. Heat Fluid Flow 94, 108919. http://dx.doi.org/10.1016/j.ijheatfluidflow.2021.108919.

Shi, B., Yang, X., Jin, G., He, G., Wang, S., 2019. Wall-modeling for large-eddy simulation of flows around an axisymmetric body using the diffuse-interface immersed boundary method. Appl. Math. Mech. 40 (3), 305–320. http://dx.doi.org/10.1007/s10483-019-2425-6.

Stern, F., Yang, J., Wang, Z., Sadat-Hosseini, H., Mousaviraad, M., Bhushan, S., Xing, T., 2013. Computational ship hydrodynamics: Nowadays and way forward. Int. Shipbuild. Prog. 60 (1–4), 3–105.

Werner, H., Wengle, H., 1993. Large-eddy simulation of turbulent flow over and around a cube in a plate channel. In: 8th Symposium on Turbulent Shear Flows. Springer, Berlin, http://dx.doi.org/10.1007/978-3-642-77674-8_12.

Yang, X., Angelidis, D., Khosronejad, A., Le, T., Kang, S., Gilmanov, A., Ge, L., Borazjani, I., Calderer, A., 2015a. Virtual flow simulator. http://dx.doi.org/10.11578/dc.20171025.1758, [Computer Software].

Yang, X., He, G.-W., Zhang, X., 2010. Towards large-eddy simulation of turbulent flows with complex geometric boundaries using immersed boundary method. In: 48th AIAA Aerospace Sciences Meeting Including the New Horizons Forum and Aerospace Exposition, Orlando, Florida.

Yang, X., Sotiropoulos, F., Conzemius, R.J., Wachtler, J.N., Strong, M.B., 2015b. Large-eddy simulation of turbulent flow past wind turbines/farms: the virtual wind simulator (VWiS). Wind Energy 18 (12), 2025–2045. http://dx.doi.org/10.1002/we.1802.

Yang, X., Zhang, X., Li, Z., He, G.-W., 2009. A smoothing technique for discrete delta functions with application to immersed boundary method in moving boundary simulations. J. Comput. Phys. 228 (20), 7821–7836.

Zhou, Z., Li, Z., He, G., Yang, X., 2021. Towards multi-fidelity simulation of flows around an underwater vehicle with appendages and propeller. Theor. Appl. Mech. Lett. 100318. http://dx.doi.org/10.1016/j.taml.2021.100318.

Zhou, D., Wang, K., Wang, M., 2020. Large-eddy simulation of an axisymmetric boundary layer on a body of revolution. In: AIAA Aviation 2020 Forum. p. 2989. http://dx.doi.org/10.2514/6.2020-2989.